

Equation of State for Solid Benzene Valid for Temperatures up to 470 K and Pressures up to 1800 MPa

Xiong Xiao^a, J.P. Martin Trusler^b, Xiaoxian Yang^a, Monika Thol^c, Saif Z.S. Al Ghafri^a, Darren Rowland^a, Eric F. May^{a*}

^a *Fluid Science and Resources Division, School of Engineering, University of Western Australia, 35 Stirling Hwy, Crawley 6009, Perth, Australia*

^b *Department of Chemical Engineering, Imperial College London, London, SW7 2AZ, UK*

^c *Thermodynamics, Faculty of Mechanical Engineering, Ruhr-Universität Bochum, Universitätsstraße 150, 44801, Bochum, Germany*

e-mail (corresponding author): eric.may@uwa.edu.au

1. Abstract

The thermodynamic property data for solid phase I of benzene are reviewed and utilized to develop a new fundamental equation of state (EOS) based on Helmholtz energy, following the methodology used for solid phase I of CO₂ by Trusler [J. Phys. Chem. Ref. Data 40, 043105 (2011)]. With temperature and molar volume as independent variables, the EOS is able to calculate all thermodynamic properties of solid benzene at temperatures up to 470 K and at pressures up to 1800 MPa. The model is constructed using the quasi-harmonic approximation, incorporating a Debye oscillator distribution for the vibrons, four discrete modes for the librons, and a further thirty distinct modes for the internal vibrations of the benzene molecule. An anharmonic term is used to account for inevitable deviations from the quasi-harmonic model, which are particularly important near the triple point. The new EOS is able to describe the available experimental data to a level comparable to the likely experimental uncertainties. The estimated relative standard uncertainties of the EOS are 0.2% and 1.5% for molar volume on the sublimation curve and in the compressed solid region, respectively; 8% to 1% for isobaric heat capacity on the sublimation curve between (4 and 278) K; 4% for thermal expansivity; 1% for isentropic bulk modulus; 1% for enthalpy of sublimation and melting; 3% and 4% for the computed sublimation and melting pressures, respectively. The equation of state also behaves physically reasonable to absolute zero and at very high-pressures.

2. Introduction

Benzene is an organic chemical compound with a ring of six carbon atoms. As a prototypical aromatic compound, benzene is one of the most studied molecules with numerous experimental studies completed and theoretical models developed.¹⁻⁸ In 2012, Thol et al. proposed a fundamental equation of state for fluid benzene from the melting curve to 725 K and at pressures up to 500 MPa.⁹ Phase diagrams in the pressure-temperature (p - T) plane are shown for benzene in Figure 1. The phase boundaries in these diagrams were constructed by combining the fluid EOS of Thol et al.,⁹ the auxiliary functions developed in this work (Section 4), and results from the literature regarding the phase behaviour of benzene at very high pressures.^{10, 11-13}

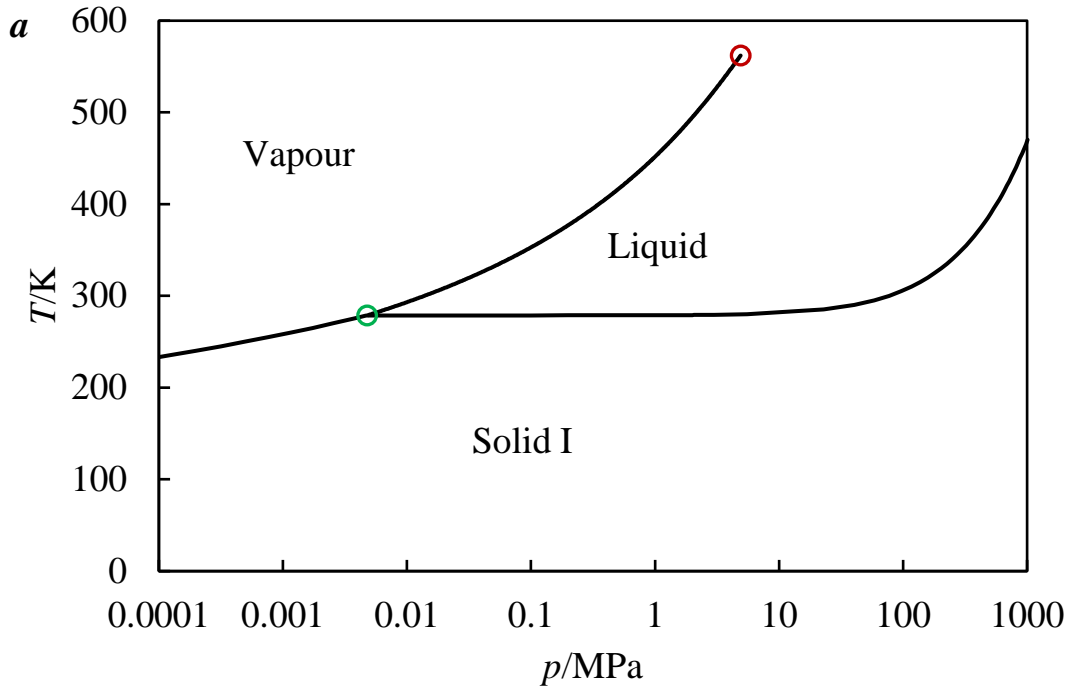


Figure 1. Pressure-temperature (T, p) diagram of benzene for **a** the solid-liquid-vapor phases based on the auxiliary functions fit to the available solid-fluid equilibrium data (detailed in Section 4) and the liquid-vapor equilibrium boundary calculated with the fluid EOS of Thol et al⁹; **b** the fluid-solid I-solid II phases, where the phase boundaries and the triple points were determined from Chanyshv et al¹⁰ with other literature.¹¹⁻¹³ The “C + H₂” region denotes where benzene decomposes. Legend: ○ critical point (562.02 K, 4.9073 MPa);⁹ ○ triple point (278.67 K, 0.00478 MPa for solid-gas-liquid triple phase point).⁹

However, there is no model available to describe accurately all the thermodynamic properties of solid benzene. The ability to calculate solid benzene’s thermodynamic properties is important in many applications. For example, in the liquefied natural gas (LNG) industry, the presence of benzene in the main cryogenic heat exchanger can lead to solid freeze-out, blockages, and ultimately LNG plant shutdowns. Significant costs (\$30 million) are associated with unplanned blockage-induced shutdowns.¹⁴ Benzene is one of the compounds of highest freeze-out risk during LNG production because it can be present in natural gas at relatively high concentrations (>1000 ppm) and it has a relatively high pure component triple-point temperature (278.67 K).¹⁵ To calculate its solubility in LNG reliably, accurate descriptions of its fugacity in the solid phase are needed at the high pressures and cryogenic temperatures relevant to LNG production.

Solid phase fugacity calculations are most commonly performed using Eq. (1), which was first proposed by Hildebrand and Scott¹⁶ and endorsed by Prausnitz.¹⁷

$$\frac{f_i^s}{f_i^l} = \exp\left[-\frac{v_i^s}{R} \left(\frac{P - P_m}{T_m} - \frac{P_m}{T_m} + \frac{C_p^l - C_p^s}{R} \ln \frac{T}{T_m}\right)\right] \gamma_i^l \quad (1)$$

where for component i , f_i^s is the solid fugacity; γ_i^l is the fugacity coefficient in the liquid phase; v_i^s refers to the enthalpy of fusion; T_m is the melting temperature; $C_p^l - C_p^s$ is the specific heat difference between liquid and solid phase; and P_m is the melting pressure. Solid-fluid equilibrium (SFE) conditions are determined by equating the solid fugacity of component i with the (partial) fugacity of that compound in the fluid (mixture). In most software packages used to calculate SFE conditions for mixtures, cubic EOS are frequently implemented to evaluate the fluid phase partial fugacities.¹⁸

In 2019, a solid solubility model for LNG-like mixtures was developed by Baker et al.,¹⁹ using the Peng-Robinson (PR) EOS for the fluid phase and the correlation from Eq. (1) for the solid phase. This model, implemented in the software tool ThermoFAST,²⁰ was regressed to the available solid-fluid-equilibrium (SFE) data for mixtures by tuning the binary interaction parameter of the PR EOS in the fluid side. Such an approach ensures that SFE predictions for binary mixtures at LNG-relevant conditions will be more accurate than those made using models tuned to VLE data.^{19, 21} However,

predictions made at conditions far from the SFE data used to tune the cubic model are less accurate. For example, Siahvashi et al. measured benzene melting temperatures that differed from the ThermoFAST predictions by between (3 and 5) K for a vapor phase methane + benzene binary at around 230 K¹⁵ and also ethane-rich ternary mixtures at around 140 K.²² Thus, an alternative and more fundamental approach for solid thermodynamic property calculations would be beneficial.

In 2011, Trusler developed an equation of state (EOS) for solid phase I of carbon dioxide in the form of a Helmholtz energy function²³ that is valid for temperatures up to 800 K and pressures up to 12 GPa. Based on the quasi-harmonic approximation, the EOS represents the available experimental data of pressure, molar volume, and isobaric heat capacity along the sublimation and melting curves, and molar volume in the compressed solid within their uncertainty. This model increases the accuracy of the solid CO₂ fugacities needed for calculations of solid-liquid equilibria with fluid mixtures, including in LNG production where CO₂ is also a compound with a high-risk of freeze-out.

Here the approach taken by Trusler for CO₂ was followed to develop an EOS for solid phase I of benzene using available property data measured along the sublimation curve, melting curve and in high-pressure regions. The resulting solid benzene EOS can be used to describe all thermodynamic properties in the solid phase I at temperatures and pressures up to 470 K and 1800 MPa, respectively. An expression for the solid's fugacity is given in Table 1 (Section 3), which can be used for SFE calculations involving mixtures. By reconciling the available thermodynamic data for solid benzene, the new model closes the gap between scientific knowledge and engineering applications. The purpose of this paper is to introduce the structure of the Helmholtz EOS for solid benzene, the method used for parameter optimization and the performance of the resulting model representing solid benzene's thermodynamic properties.

3. Thermodynamic Modelling Basis

The molar Helmholtz energy for solid benzene is described using an equation of state (EOS) with the form:

Here the subscript m denotes a molar basis, while A refers to the Helmholtz energy based on the quasi-harmonic approximation (QHA). This is a phonon-based model designed to describe volume-dependent thermodynamic properties. Further detail about A is presented in Section 3.1. The term A_{vib} is the Helmholtz energy associated with the internal molecular vibrations. In this work, the internal modes are described by an Einstein approximation. The internal modes depend weakly on crystal volume via its influence on vibrational frequencies. Details about A_{vib} are presented in Section 3.2. The anharmonic term, A_{anh} , for the Helmholtz energy corrects for various deviations between the QHA and the actual behavior of crystals. A description of A_{anh} is given in Section 3.4.

All the thermodynamic properties of the solid crystal can be derived from the Helmholtz energy A via differentiation.²³ Table 1 lists the relationships between each thermodynamic property, the Helmholtz energy and its various derivatives. These relationships were used in the regression of the EOS to the various experimental data sets for different solid phase properties.

Table 1. Thermodynamic properties in terms of the Helmholtz energy A , where N is the number of molecules, and V is the volume.

Property	Symbol	Relationship to A	
Internal energy	U	—	(3)
Entropy	S	—	(4)
Pressure	p	—	(5)
Gibbs free energy	G		(6)
Enthalpy	H		(7)
Isochoric heat capacity	c_v	—	(8)
Isobaric heat capacity	c_p	— — —	(9)
Thermal expansivity		— — —	(10)
Isentropic compressibility	K_S	— —	(11)
Fugacity coefficient		— — — — — — —	(12)

Note: Here A^0 , A^0_{ideal} , and A^0_{ideal} is the ideal gas Helmholtz energy where no intermolecular forces exist. A formulation for A^0_{ideal} is given in Eq. (3) of Thol et al.⁹

3.1. The Quasi-Harmonic Approximation

As detailed by Trusler,⁹ the spirit of the quasi-harmonic approximation is to describe crystalline solid lattice vibrations via independent harmonic oscillators, the frequencies of which are only related to the lattice volume. According to the QHA model,²⁴ at temperature T , the configurational Helmholtz energy A for a crystal of volume V with N molecules is given by:

$$A = A^0 + \sum_{\mathbf{q}, \nu} \frac{h\nu_{\mathbf{q}, \nu}}{2} + k_B T \sum_{\mathbf{q}, \nu} \ln \left[1 - \exp\left(-\frac{h\nu_{\mathbf{q}, \nu}}{k_B T}\right) \right]^{-1} \quad (13)$$

Here ω_l is the angular frequency of the l^{th} harmonic lattice mode for phonons of wavevector k , \hbar is the reduced Plank constant defined as $\hbar = h/2\pi$, and $\phi(r)$ is the effective pair-potential-energy function for a specific crystal structure that is dependent on r .

The intermolecular potential energy and zero-point lattice vibrational lattice energy can be combined into a single term for the total configurational energy at zero temperature. This combination gives rise to the so-called “cold curve” function described below.

The third term in Eq. (13), the summation of external lattice vibrations, may be evaluated in principal via integration using a density of states function, $\rho(\omega)$:

$$E_{\text{ext}} = \int_0^{\infty} \hbar \omega \rho(\omega) d\omega \quad (14)$$

where $E_{\text{int}}(0)$ is the total configurational internal energy at zero temperature, while m and n are the numbers of external degrees of freedom and molecules per unit cell, respectively. The density of states is normalized as:

$$\int_0^{\infty} \rho(\omega) d\omega = m \quad (15)$$

The construction of the density of states serves as a bridge between the crystal’s molecular structure and the representation of its properties with a thermodynamic model. A convenient way to develop the density of states function is to anchor a physical model for the various modes to the unit cell of the crystal lattice.

The benzene molecule belongs to the D_{6h} point group, possessing a main C_6 axis, perpendicular to the planar molecule, six C_2 axes perpendicular to the C_6 axis, three symmetry planes and a center of inversion. As shown in Figure 2, the principal axes coincide with the central C_6 axis, with one set of C_2 axes passing through opposing carbon atoms and one set of C_2 axes passing through opposing C-C mid-bonds.

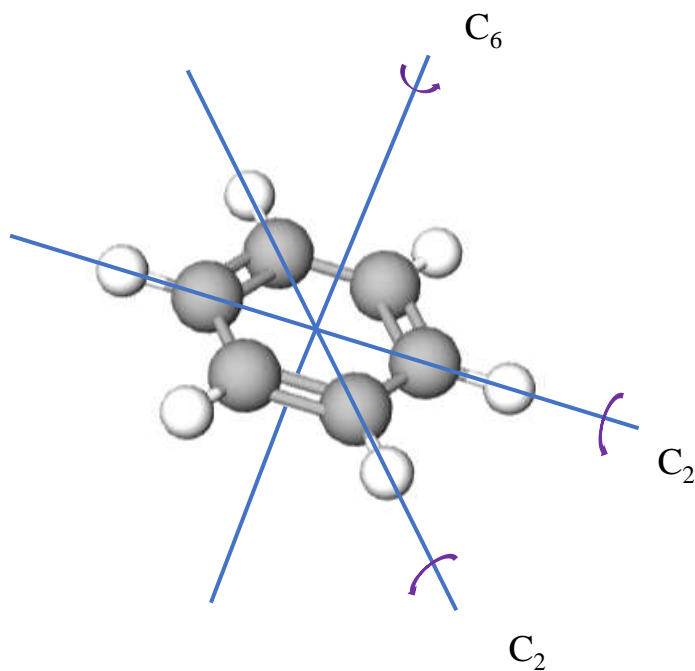


Figure 2. Principal axes for the benzene molecule: in-plane C_2 axes and the mutually-orthogonal C_6 axis. In this plot two C_2 axes are shown as representatives of the two sets of C_2 axis (one set passing through the carbon atoms at opposing vertices and one set passing through the bonds that make up opposing edges of the molecule).

As shown in Figure 3, benzene solid phase I is a face-centered orthorhombic structure. Orthorhombic lattices stem from stretching a cubic lattice along two orthogonal axes. This results in a rectangular prism with a rectangular base ($a_1 \times a_2$) and height (a_3), such that a_1 , a_2 , and a_3 are distinct and mutually orthogonal. For benzene solid phase I, the unit cell is centrosymmetric and at 270 K the cell parameters are $a_1 = 7.460 \text{ \AA}$, $a_2 = 7.034 \text{ \AA}$ and $a_3 = 9.666 \text{ \AA}$.²⁵

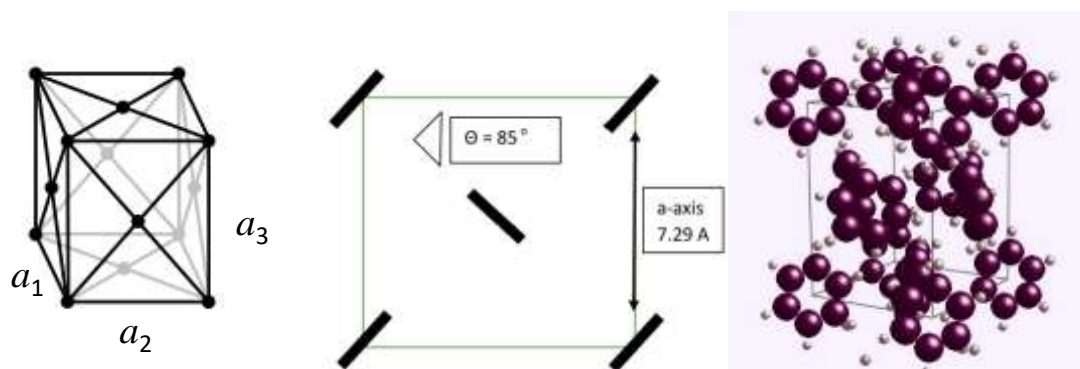


Figure 3. (left) Orthorhombic unit cell from the crystal structure of solid phase I benzene.²⁶ (center) Structure of the unit cell looking down the c -axis with planar molecules seen side on.²⁵ (right) Visualization of the unit cell with indicative atom locations.²⁷

Molecular centers of mass are located at the 8 corners and in the centers of the 6 faces, resulting in there being 4 molecules in the unit cell ($8 \times 1/8 + 6 \times 1/2$). With four molecules in the unit cell and 12 atoms per molecule there are $N = 48$ atoms and $3N = 144$ degrees of freedom per unit cell. For this number of external degrees of freedom, the complete density of states function would be extremely difficult to construct. However, it may be sufficient to use a simplified analysis based on an approximation in which (a) the unit of analysis remains the molecule (rather than the unit cell) and (b) the molecules are considered to move in a fixed, mean potential-energy field provided by the crystal as a whole. This leads to 36 degrees of freedom (modes) per molecule.

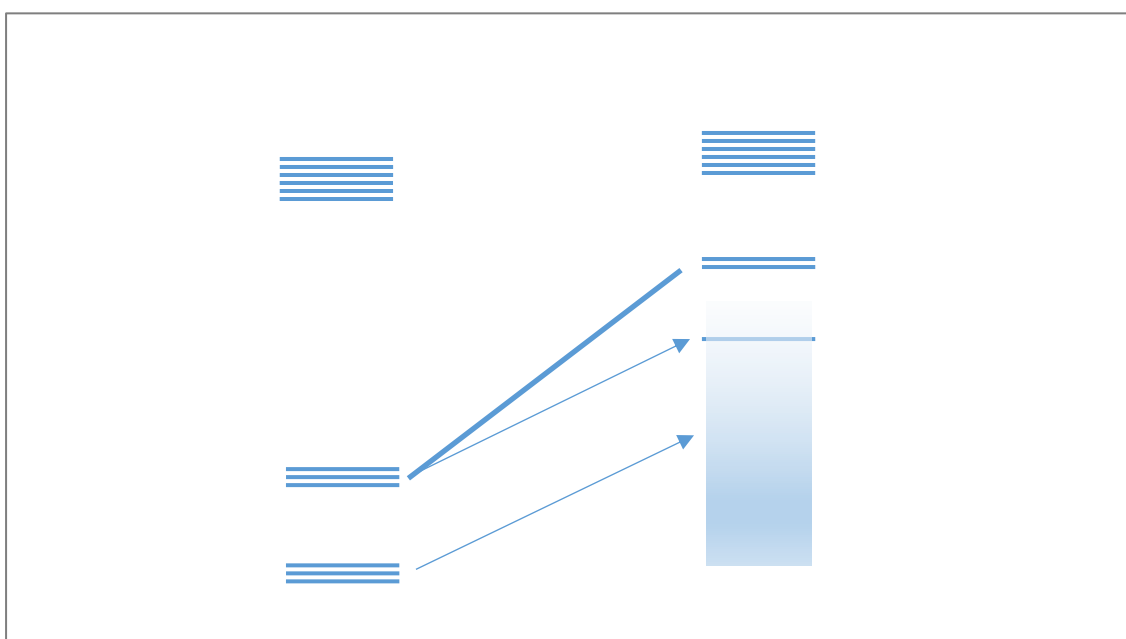


Figure 4. Conjectured correlation between the modes of motion of C_6H_6 molecules in the gas phase and in the crystal.

As indicated in Figure 4, an initial analysis begins with the assumption that the degrees of freedom for a benzene molecule in the gas phase can be mapped to one in the crystal with 30 internal and 6 external modes. The internal vibrations of the molecule are retained in the solid with oscillator frequencies different from those of the external modes. The energy for the internal modes is represented by the ϵ_{int} term in Eq. (2). The translational modes of the isolated molecule (as observed in the gas phase) translate into three pseudo-vibrational lattice modes ('vibrons' or phonons), while the rotational modes around the different C_2 principal axes translate into two librational modes, and the one rotational mode around the C_6 principal axis translated to a torsional

(or hindered rotational) mode. In the Debye-Einstein approximation, the vibrons are approximated by a Debye distribution, and the librations (a reciprocating motion in which an object rotates repeatedly back and forth about an almost fixed axis²⁸) are represented by discrete harmonic terms modelled by the Einstein function. The torsional mode is also regarded as harmonic and described by a discrete Einstein term.

To determine the number of modes in each category, benzene symmetry and spectroscopic information in the literature were considered. Thiéry and Léger reported that there are three Raman active librational modes ($3 \times C_2$ axis) for the benzene molecule.²⁹ Another Einstein term is needed to describe the torsional mode because there is only one C_6 axis per molecule. The remaining two external degrees of freedom are attributed to vibrons as described by the Debye distribution. Thus, the density of states is constructed with a weighting of 1/3 on the Debye distribution for vibrons and 2/3 on the discrete harmonic terms for torsion and librations. The expression for the density of states based on the Debye-Einstein approximation:³⁰

$$\text{---} \tag{16}$$

Here ω_D is the angular cut-off frequency of the Debye distribution, $H(x)$ is the Heaviside step function^a, $\delta(x)$ is the Dirac delta function, M is the number of discrete harmonic modes, ω_i and a_i are respectively the angular frequency and the weight of the i^{th} discrete harmonic term, and ω_D^3 . (Note: the factors of 3 associated with the 1/3 weight for Debye distribution and the default Debye density of states, $\frac{3}{4\pi^2} \frac{\omega^3}{v^3}$, cancel.)

By considering two Debye modes and four Einstein modes (three librational and one torsional modes) for the benzene crystal, the QHA for the molar Helmholtz energy may then be expressed as:

$$\tag{17}$$

^a $H(x) = 0$ for $x < 0$ and $H(x) = 1$ for $x \geq 0$.

Here, V_m is the molar volume, ϕ is the cold curve function for the Helmholtz energy of the system at absolute zero, ϕ_D corresponds to the Debye distribution and ϕ_{lib} represents the librational and torsional modes.

Since no experimental data are available at absolute zero, all the properties represented by the cold curve are computed via extrapolation of the sublimation curve from above zero temperature. To represent the compression behavior of the solid at absolute zero with sufficient precision, a fourth-order logarithmic equation of state suggested by Poirier and Tarantola³¹ was used in this work. The molar Helmholtz energy along the cold curve is then expressed by:

$$\phi = \phi_D + \phi_{lib} + \phi_{lib} \quad (18)$$

where z is the reduced density ($z = V_m/V_0$), V_0 is the molar volume of the crystal at zero temperature and pressure, while c_1 , c_2 and c_3 are parameters related to the bulk modulus of the cold crystal and its first two derivatives with respect to pressure.³²

The Helmholtz energy of the Debye distribution for lattice vibrations is:^{30, 33}

$$\phi_D = \frac{3}{8\pi^2} \left(\frac{3k_B T}{\theta_D} \right)^3 \int_0^{\theta_D/k_B T} \frac{x^3}{e^x - 1} dx \quad (19)$$

Here θ_D is the characteristic temperature for the Debye distribution with the definition of $\theta_D = \hbar \omega_D / k_B$. Physically, it reflects the energy associated with the highest normal vibrational mode of a crystal, and links the solid's elastic properties to its thermodynamic properties including thermal expansion, heat capacity and enthalpy.³⁴ Importantly, the characteristic temperature for the Debye distribution depends on crystal volume as detailed below, while θ_D is the Debye function:

$$- \quad - \quad (20)$$

The Helmholtz energy associated with each librational and torsional mode is given by:³⁰

33

$$- \quad (21)$$

Here θ_i is the characteristic temperature for each Einstein mode defined by $\theta_i = \hbar \omega_i / k_B$. The characteristic temperatures for the librational and torsional mode also depend (in principle) on crystal volume, as characterized by the Grüneisen parameters detailed in Section 3.3.

3.2. Internal Modes

There are thirty internal modes for an isolated benzene molecule: ten single and ten doubly-degenerate modes, as shown in Table 2. These modes can be identified via the infrared and Raman spectra observed for the solid phase I.^{29, 35-48} In this work, each internal mode is described by the Einstein approximation and thus their contribution to the crystal's Helmholtz energy is given by the following two equations:

$$(22)$$

$$- \quad (23)$$

where Ω is the total number of internal modes, ω_i represents the weighting of the single ($\omega_i = 1$) or the doubly-degenerate ($\omega_i = 2$) modes, and θ_i is the Einstein characteristic temperature for the internal modes. Each θ_i is a constant, or a weakly dependent function of volume, with all parameters determined from spectroscopy.

3.3.Grüneisen Parameters

The Grüneisen parameter represents the thermal pressure from a collection of vibrating atoms with the general definition of

$$\gamma = \frac{\alpha}{\beta} \frac{1}{C_V} \left(\frac{\partial C_V}{\partial \ln V} \right)_T \quad (24)$$

The dependence of the characteristic temperatures on crystal volume can be quantified via the Grüneisen parameters:

$$\theta_j = \theta_{j0} \left(\frac{V}{V_0} \right)^{\gamma_j} \quad (25)$$

$$\theta_j = \theta_{j0} \left(\frac{V}{V_0} \right)^{\gamma_j} \quad (26)$$

The Grüneisen parameters themselves vary with the expansion or compression of the crystal, and this variation may be approximated via an empirical model:

$$\gamma_j = \gamma_{j0} + \gamma_{j1} \left(\frac{V}{V_0} \right)^{\gamma_{j2}} \quad (27)$$

$$\gamma_j = \gamma_{j0} + \gamma_{j1} \left(\frac{V}{V_0} \right)^{\gamma_{j2}} \quad (28)$$

Here γ_{j0} and γ_{j1} are the corresponding Grüneisen parameters at zero temperature, and γ_{j2} and γ_{j3} are exponents specific to each mode, which need to be determined when constructing an EOS. The characteristic temperatures at a specific molar volume V_m are then expressed as

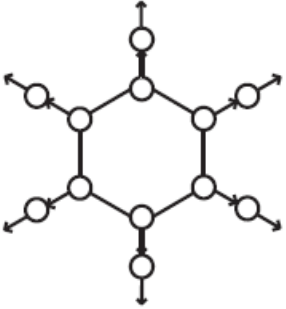
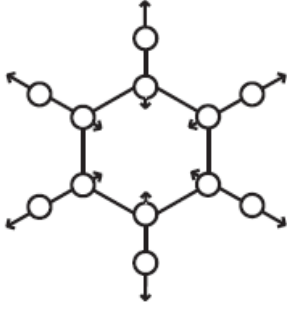
$$\theta_j = \theta_{j0} \left(\frac{V_m}{V_0} \right)^{\gamma_{j0} + \gamma_{j1} \left(\frac{V_m}{V_0} \right)^{\gamma_{j2}}} \quad (29)$$

$$\theta_j = \theta_{j0} \left(\frac{V_m}{V_0} \right)^{\gamma_{j0} + \gamma_{j1} \left(\frac{V_m}{V_0} \right)^{\gamma_{j2}}} \quad (30)$$

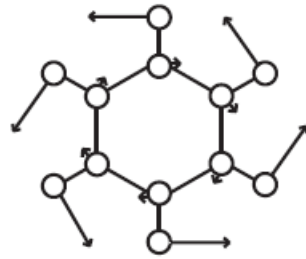
In cases where the exponent vanishes (e.g. $\nu = 0$), the expressions simplify (e.g. $\gamma = 1$). The α and β are written as α_0 and β_0 in Eqs. (21) and (23), respectively.

The Grüneisen parameters for the external modes were determined via regression of ten parameters: the Debye mode coefficients (α_0 , β_0) and the four pairs of Einstein mode coefficients (α_1 and β_1). The Grüneisen parameters for the internal modes were not fitted but were instead obtained from the spectroscopic literature or were estimated when only very few data were available for a given mode based on the values known for other modes. The Grüneisen parameter and the values of α and β can be determined from the frequencies ν of each mode via $\alpha = \frac{\nu}{\nu_0} \frac{d\nu_0}{dT}$ and $\beta = \frac{\nu}{\nu_0} \frac{d\nu}{dT}$. Table 2 lists the internal modes of the benzene molecule together with their corresponding frequency (wavenumber) and characteristic temperature.

Table 2. Internal modes for benzene labelled with Wilson notation.⁴⁹ The representation of all modes comes from Figure 1 of Gardner and Wright.⁵⁰ Those labelled with “a” and “b” are degenerate modes, and others are single modes.

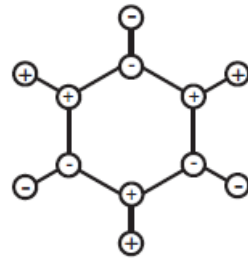
No.	Notation	ν/cm^{-1}
1		992 (195 K) ³⁹
2		3065 (195 K) ³⁹

3



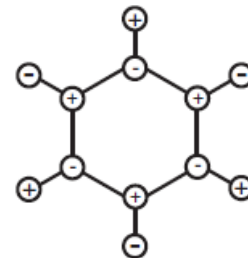
1350 (270.15 K)⁴⁰

4



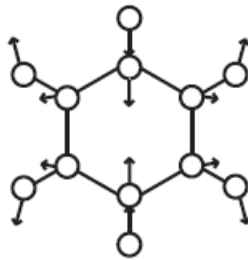
704 (261.15 K)³⁵

5



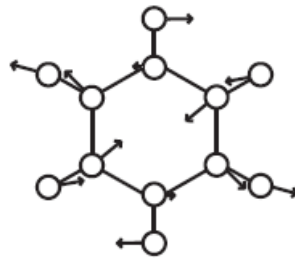
996 (216.15 K)³⁵

6a

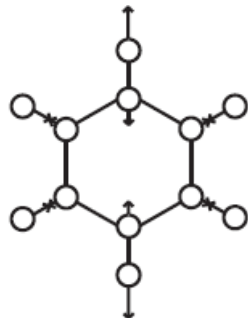


607 (270.15 K)⁴⁰

6b

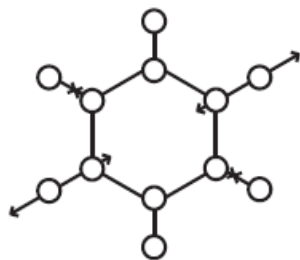


7a

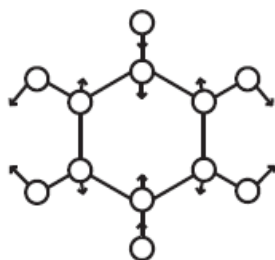


3055 (270.15 K)⁴⁰

7b

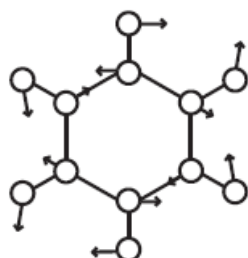


8a



1600 (270.15 K)⁴⁰

8b

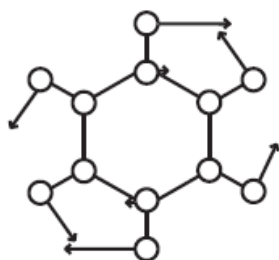


9a

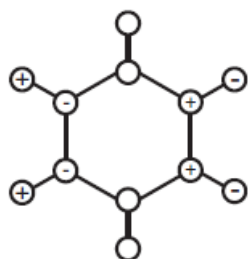


1170 (261.15 K)³⁵

9b

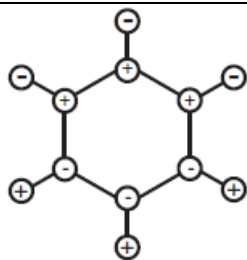


10a

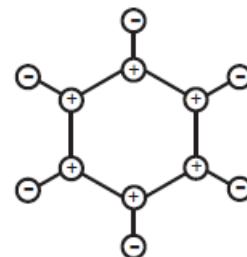


859 (261.15 K)³⁵

10b

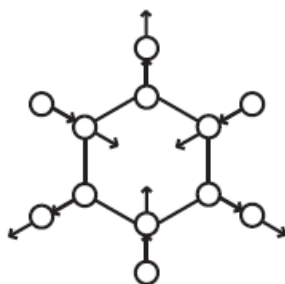


11



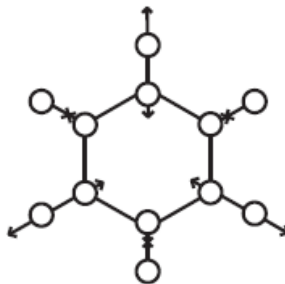
685 (261.15 K)³⁵

12



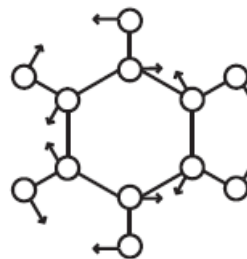
1010 (261.15 K)³⁵

13



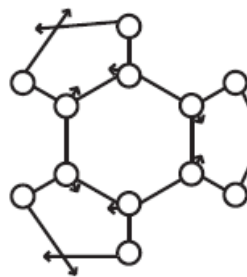
3070 (261.15 K)³⁵

14



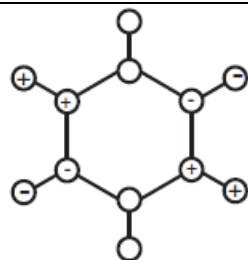
1311 (261.15 K)³⁵

15



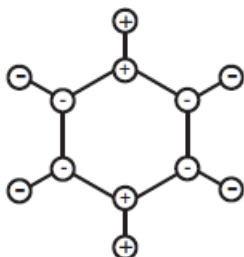
1147 (261.15 K)³⁵

16a

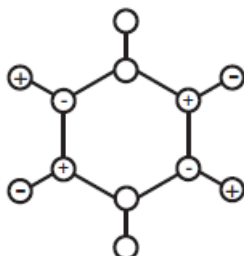


405 (261.15 K)³⁵

16b

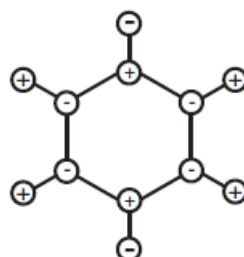


17a

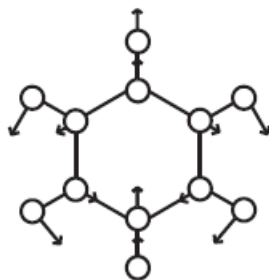


975 (261.15 K)³⁵

17b

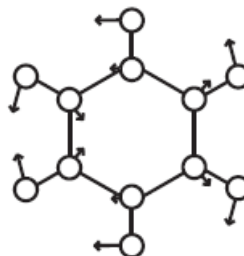


18a

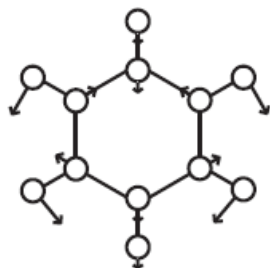


1036 (261.15 K)³⁵

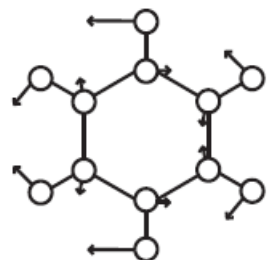
18b



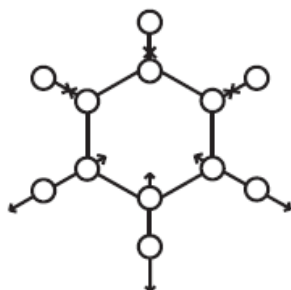
19a

1478 (261.15 K)³⁵

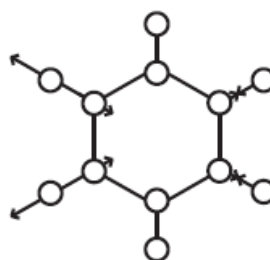
19b



20a

3081 (261.15 K)³⁵

20b



No comprehensive study of the variation with pressure of the frequencies, and thus the Grüneisen parameters, exists for all modes at different temperatures. However, Thiéry and Léger did report on the variation of seven frequencies (, , , , , and) with pressure up to 1516 MPa for the solid phase I of benzene at 294 K.²⁹ To calculate their characteristic temperatures at and the corresponding Grüneisen parameters, these seven wavenumbers were examined as functions of the molar volume estimated by Katrusiak et al.⁵¹ from an isothermal chart at 295 K. The molar volume of the crystal is relatively insensitive to temperature and the change caused by considering 295 K instead of 294 K is negligible. The value of obtained from extrapolation of the literature data^{52, 53} is 69.80 cm³/mol. As indicated in Figure 5,

$\ln(\nu_1)$ and $\ln(V_m/V_{00})$ show a linear relationship. This dependence also applies to the other six frequencies. It was assumed that $\gamma_1 = 0$ for all modes so that Eq. (28) becomes $\ln(\nu_1) = \ln(\nu_{1,0}) - \beta_1 \ln(V_m/V_{00})$, and the Grüneisen parameters determined at 294 K can be used at any temperature.

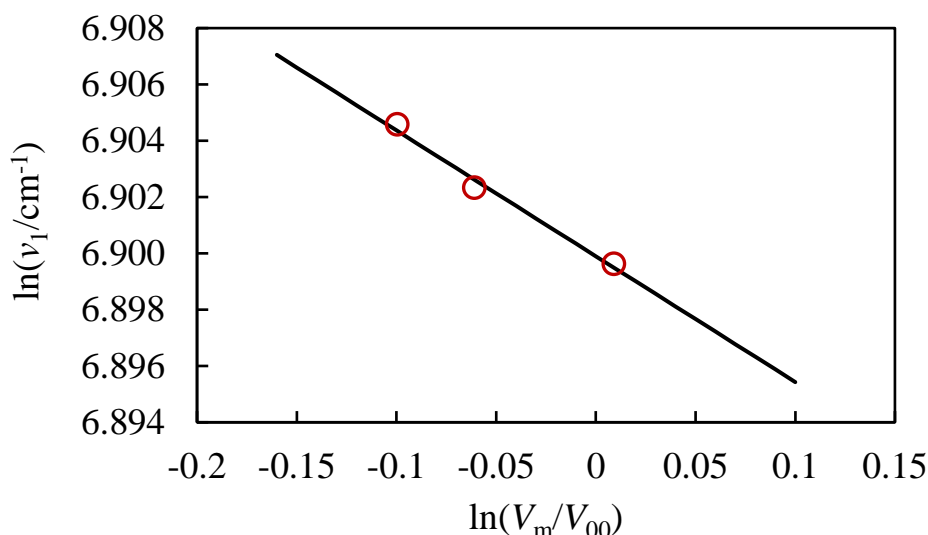


Figure 5. Wavenumber ν_1 (frequency of one internal mode) for solid benzene at 294 K as a function of molar volume. \circ : experimental data from Thiéry and Léger;²⁹ the black solid line is the linear regression. V_{00} refers to the zero temperature cell volume.

The limited data available in the literature for other internal modes means their dependence on molar volume cannot be calculated. For these modes, the corresponding values of the Grüneisen parameters and exponents were set to be zero with the supposition that the characteristic temperatures for these internal modes do not vary with molar volume. For each wavenumber, β_i was computed from the averaged reported frequency ν_i . Satisfactory results for all thermodynamic properties were achieved using this assumption.

3.4. Anharmonic Term

Significant deviations from the QHA model are to be expected, especially in the region near the triple point and at high temperatures where the crystal volume is largest. This is even more true for benzene in comparison with other models of pure molecular solids based on the QHA, like CO_2 , because benzene has a comparatively complex structure.

A renormalization method to correct the QHA for anharmonic effects was developed by Wu and Wentzcovitch⁵⁴ for metal oxides. They found that a single temperature and volume dependent parameter was sufficient to capture anharmonic effects. In the development of a Helmholtz EOS for solid CO₂, Trusler followed this method, stating that the correction to the Helmholtz energy varies as T^{-4} at low temperatures^{23, 55} and could be represented with the following expression:

$$\frac{\text{---}}{\text{---}} \text{---} \quad (31)$$

Here three more parameters b_1 , b_2 and b_3 are introduced. The anharmonic effect for solid benzene is represented by the above equation which depends exponentially on changes in molar volume. At high temperatures, the anharmonic correction quantifies the departure from the Dulong-Petit limit⁵⁶ for the lattice heat capacity: a negative (positive) value of b_1 means the deviation is positive (negative).

3.5. Thermodynamic Property Functions Derived from the Helmholtz Energy A

In this section, the expressions for each of the thermodynamic properties listed in Table 1 are given in terms of the contributions considered in Eq. (2). For any molar thermodynamic property, Z_m :

$$(32)$$

This can be further expanded as:

$$(33)$$

When deriving explicit expressions for each of the thermodynamic properties in Table 1, it is convenient to define the following functions:

$$\frac{\bar{u}}{\bar{v}} \quad (34)$$

$$\frac{\bar{u} \quad \bar{v}}{\bar{v}} \quad (35)$$

$$\frac{\bar{u} \quad \bar{v} \quad \bar{v}}{\bar{v}} \quad (36)$$

$$\bar{v} \quad (37)$$

Then each of the terms in Eq. (33) can be written for each thermodynamic property as follows:

for the internal energy U ,

$$(38)$$

$$(39)$$

$$(40)$$

$$(41)$$

for entropy S ,

(42)

(43)

(44)

(45)

for pressure p ,

(46)

(47)

(48)

(49)

and for isochoric heat capacity c_v ,

(50)

(51)

(52)

(53)

The isobaric heat capacity, isotropic compressibility and thermal expansivity can then be evaluated using the partial derivatives $\left(\frac{\partial T}{\partial p}\right)_S$ and/or $\left(\frac{\partial S}{\partial p}\right)_T$:

$$\frac{\frac{\frac{\quad}{\quad}}{\quad}}{\quad} \quad (54)$$

$$\frac{\frac{\quad}{\quad}}{\quad} \quad (55)$$

$$\frac{\frac{\frac{\quad}{\quad}}{\quad}}{\quad} \quad (56)$$

Each of the terms in Eq. (33) needed for $\frac{\quad}{\quad}$ and $\frac{\quad}{\quad}$ are then determined as follows:

$$\frac{\quad}{\quad} \quad (57)$$

$$\frac{\quad}{\quad} \quad (58)$$

$$\frac{\frac{\frac{\quad}{\quad}}{\quad}}{\quad} \quad (59)$$

$$\frac{\frac{\frac{\quad}{\quad}}{\quad}}{\quad} \quad (60)$$

$$\frac{\quad}{\quad} \quad (61)$$

$$\frac{\quad}{\quad} \quad (62)$$

$$\frac{\quad}{\quad} \quad (63)$$

$$\frac{\quad}{\quad} \quad (64)$$

Here $\left(\frac{\partial G}{\partial V}\right)_T$ is the first derivative of G , and the prime refers to the derivative with respect to V .

4. Auxiliary Function

The sublimation and melting pressures of solid benzene were obtained by solving the equality of Gibbs free energy between the fluid equation of state from Thol et al.⁹ and this fundamental equation for the solid. The original reference EOS for fluid benzene⁹ does not cover conditions below the triple point or densities above 11.45 mol/dm³ as required in the vicinity of the solid phase equilibrium curves. There is also an upper pressure limit at 500 MPa. To obtain Gibbs energies at SFE conditions from the reference fluid EOS, the fluid model was extrapolated in this work to the necessary conditions of temperature and density (or pressure). Numerical values produced by this extrapolation are provided in the Supplementary Information as part of the Excel sheet labelled “Benzene sample calculation”.

During the development of this solid model, auxiliary functions for sublimation and melting were proposed to estimate initial phase equilibrium pressures for saturated property calculations. Parameters from the two auxiliary equations were regressed to the same experimental data that were fitted to the EOS as described in Sections 6.1 and 6.2. In this approach, one degree of freedom is eliminated as temperature and equilibrium pressure are input to the property regression along the sublimation and melting curves. Auxiliary functions also enable users to quickly calculate the solid-fluid equilibrium condition by simply entering temperature.

For the sublimation curve, the equation is expressed as:

$$\ln\left(\frac{p}{p^*}\right) = \frac{v_s}{RT} - \frac{v_f}{RT} - \frac{u_s}{RT} + \frac{u_f}{RT} - \frac{p v_s}{RT} + \frac{p v_f}{RT} \quad (65)$$

where T_3 and P_3 are the triple point temperature (278.67 K) and pressure (0.00478 MPa);
 $\alpha = -19.47$, $\beta = -0.75865$ and $\gamma = -61.633$.

For the melting curve, the auxiliary function is:

$$- \quad - \quad - \quad - \quad (66)$$

The coefficients are $A = 92000$ and $B = 254000$.

Equations (65) and (66) are valid over the temperature ranges of (193 to 278.67) K and (278.67 to 363) K, corresponding to the respective ranges of available experimental data. The functional forms allow the two formulations to meet at the triple point. Results are discussed in Sections 6.1 and 6.2.

5. Parameter Optimization

The parameter optimization process followed the method used by Trusler for solid CO₂.²³ However, one major difference with and CO₂ is that there are very limited bulk modulus data for solid benzene and thus no pre-fitting process regarding the bulk modulus was performed. For solid CO₂, the pre-fitting process had two purposes: to determine the number of librational modes and to provide an estimated value for β . Here, for solid benzene, the number of librational modes was fixed as stated in Section 3.1, and the value of β was regressed directly in the global fitting procedure.

The first step is to identify parameters that can be determined independently of the regression. As detailed previously, the characteristic temperatures of the internal modes were taken from the spectroscopic data; the corresponding Grüneisen parameters were either calculated from the experimental data or set to be zero in cases where insufficient measurements exist. Similar to the solid CO₂ EOS, all the Grüneisen exponents are set to be zero. Parameters for the internal modes are given in Table 3.

Table 3. Parameters that were not regressed for this equation of state.

Parameter	Value	Parameter	Value
$/(cm^3 \cdot mol^{-1})$	69.80	d_1 to d_5	1
to	0	d_6 to d_{10}	2
	3	d_{11} to d_{15}	1
	1	d_{16} to d_{20}	2
$/K$	1427.4		0.0447
$/K$	4415.3		0.0331
$/K$	1942.3		0
$/K$	1014.8		0
K	1456.6		0.051
$/K$	872.3		0.0046
$/K$	4384.1		0.0299
$/K$	2311.4		0.0202
$/K$	1703.8		0.0256
$/K$	1239.0		0
$/K$	989.5		0
$/K$	1453.2		0
$/K$	4398.3		0
$/K$	1886.3		0
$/K$	1650.5		0
$/K$	587.5		0
$/K$	1407.7		0
$/K$	1490.6		0
$/K$	2126.7		0
$/K$	4421.3		0

Here, θ_i and α_i refer to the Einstein characteristic temperature, Grüneisen exponents, and Grüneisen parameters for each internal mode. Coefficients of a_i and d_i are the weight for i^{th} discrete harmonic term for librational/torsional modes and internal modes.

The next step is to define the number of parameters required for the QHA and anharmonic corrections. As discussed in Section 3.1, there are four Einstein modes (three for libration and one for torsion) in the QHA model. Nonetheless, the three librational modes might share the same characteristic temperature and Grüneisen parameter. Considering there are three parameters (characteristic temperature, Grüneisen parameter and Grüneisen exponent) for each mode, over-fitting might occur if all the twelve variables are used. In the initial stage, it was assumed that there are only two different characteristic temperatures with independent Grüneisen parameters and exponents in the external Einstein model: one for the librational and the other for the torsional mode, respectively. Thus, fifteen parameters needed to be regressed in the initial stage (six from the librational and torsional modes, three from the Debye distribution, three from the cold curve and three from the anharmonic correction) to the measured thermodynamic properties. The coefficients were assumed to be θ_{lib} for libration and θ_{tors} for torsion. Additionally, the value of the gas-phase entropy at the triple point anchors the solid's enthalpy and has a significant influence on the phase equilibrium pressure calculations performed with the fluid model. Since the absolute value of enthalpy or entropy between equilibrium states cannot be observed experimentally, a reference value $S_m(g, T_t, p_t)$ may be assigned for the gas phase entropy at the triple point as part of the tuning process without influencing any of the calculated solid properties. At the triple point, the differences in the entropy and enthalpy between the fluid and the solid ($\Delta S_{m,fluid}$ and $\Delta H_{m,fluid}$), were computed as:

$$(67)$$

$$(68)$$

where $S_m(g, T_t, p_t)$ is the molar entropy at the triple point calculated from the reference fluid EOS, $G_m(g, T_t, p_t)$ refers to the molar Gibbs free energy at the triple point calculated from the solid model, and $H_m(g, T_t, p_t)$ is the molar enthalpy at the triple point calculated from the reference fluid EOS. At a given (T, p) condition, $\Delta S_{m,fluid}$, $\Delta H_{m,fluid}$, and $\Delta G_{m,fluid}$ were calculated as:

(69)

(70)

Here h^f and g^f are respectively the molar enthalpy and Gibbs free energy from the fluid model, and h^s and g^s are those from the solid EOS. Phase equilibrium exists where $g^f - g^s$ becomes zero. Values of h^f and g^f can also be determined via Eqs. (69) and (70).

In total, sixteen parameters were adjusted to fit all the available thermodynamic properties. The global fit was achieved via minimization of the objective formulation given below:

$$\sum_{i=1}^N \sum_{j=1}^M w_{ij} (X_{ij}^{\text{exp}} - X_{ij}^{\text{calc}})^2 \quad (71)$$

where X refers to a thermodynamic property, X_{ij}^{exp} is the i^{th} experimental data point for the property (j) where j refers to the listed property in Table 4, X_{ij}^{calc} is the calculated value for property (j) at condition i from the equation of state, w_{ij} is the weighting factor for that data point, and N is the total number of data points tuned. Additionally, limiting constraints were used in the fit to ensure that the behavior of the EOS was physically reasonable within the range of validity where no data exist.

The values used for the weighting factors are empirical and were determined by the scale of the RMS deviation, the uncertainty of experimental data (if stated in the corresponding publication) as well as their location in the solid-phase region, and the sensitivity of each property in the regression. For enthalpies of sublimation and melting, and phase equilibrium calculations, the weighting factors are also influenced by the enthalpy and Gibbs free energy values computed from the fluid model. In this work, different literature sources for a given thermodynamic property were generally treated equally because there is no obvious evidence that some data are of higher quality than others. However, data that were read from a plot or are clearly of lower accuracy were

assigned half the w_i values of others. Additionally, two different weighting factors were used for heat capacities above and below 200 K because otherwise, the fitting at high temperatures would deviate excessively in absolute terms even when the relative differences are small: $c_{p,m}(T \rightarrow 0) \rightarrow 0$, while $c_{p,m}(T = 200 \text{ K})$ and $c_{p,m}(T = 270 \text{ K})$ are approximately (84 and 123) $\text{J}\cdot\text{K}^{-1}\cdot\text{mol}^{-1}$. The thermodynamic property regression to the low temperatures was performed by restricting the thermal expansivity to be positive when $T \rightarrow 0$. The Grüneisen parameter was also constrained to be close to the value of γ at temperatures between (0 and 30) K: as stated by Trulser,²³ γ is expected to reach the value of γ_D as γ_D under the Debye-Einstein approximation. This helped avoid unphysical property calculation results and anomalous values of γ . At high pressures, the model's behavior is physically reasonable and no further regression was performed. Values of w_i used in the regression are tabulated in Table 4, where the subscript denotes the specific property to which the weighting factor refers.

Table 4. List of weighting factors used for thermodynamic property regression and low temperature behavior. The subscript denotes the property to which the weighting factor was applied.

	Property	Value
Sublimation		1
		3
		10
		3
	a	3
		3
		3
Melting		3
Single-phase data measured at high-pressure		1
		3
Low temperature behavior		1
		1

a. Enthalpies of sublimation and melting were fitted together.

The regression was performed by fitting to one property at a time in sequence until all were represented adequately. The impact of each parameter on each thermodynamic property was studied as shown in Table 5. In the initial stages of fitting, only the Grüneisen parameters and exponents q were tuned to the molar volume V_m . Characteristic temperatures and anharmonic factors b_1 to b_3 were then included when fitting to heat capacities. It was found that the thermal expansivity could be fit adequately with these four types of parameters as well. The cold curve parameters c_1 to c_3 were then added to describe the isentropic bulk modulus, and the gas entropy value at triple point was utilized for enthalpy and phase equilibria descriptions. Ultimately, sixteen tuned parameters allow the EOS to compute properties in excellent agreement with the experimental data, satisfy reasonable physical behavior where there is no data, and keep the exponent values small. The best fit parameters are listed in Table 6. Compared with the values in Table 3, the Grüneisen parameters for the external modes are much larger than those for the internal modes, which indicates that the are comparatively insensitive to variations in the molar volume, as might be expected.

Table 5. List of the parameters and the effect on thermodynamic properties

Parameters	Most sensitive properties	Notes
c_1 and c_2	and K_S	c_p , α , H , G_{sub} and G_{melt} (mild impact)
c_3		Small impact on all properties
b_1 , b_2 and b_3	c_p and H	α , K_S , G_{sub} and G_{melt} (mild impact)
q_1 , q_2 and q_3	Almost all properties	
b_1 , b_2 and b_3	α , H , G_{sub} and G_{melt}	
c_1 , c_2 and c_3	Almost all properties	
$S_m(g, T_t, p_t)$	H , G_{sub} and G_{melt}	

Table 6. Best-fit parameter values for the optimized solid benzene equation of state.

Parameter	Value
c_1/MPa	7011
c_2/MPa	17963
c_3/MPa	76005
	101.1
	140.2
	130.4
$S_m(\text{g}, T_t, p_t) / (\text{J}\cdot\text{mol}^{-1}\cdot\text{K}^{-1})$	291.93
q_D	-5
	-5
	5
	2.96
	0.368
	9.25
b_1	-0.0094
b_2	0.053
b_3	0.17

6. Comparison with Data

Results of the fit for each individual property are summarized in Table 7 to Table 9, with data separated into the phase-change measurements on the sublimation curve and on the melting curve, and the high pressure single-phase region. Inconsistent data that are obviously outliers were excluded in the regression process. The statistical measures of absolute average relative deviations (AAD) and root mean square (RMS) deviation for a given property (j) were calculated via the following equations:

$$\frac{\sum_{i=1}^n |y_i - \hat{y}_i|}{\sum_{i=1}^n y_i} \quad (72)$$

$$\frac{\sum_{i=1}^n \frac{1}{x_i}}{n} \quad (73)$$

Here n is the total number of points considered for a literature data source reporting a given property (j).

6.1. Data on the Sublimation Curve

For solid benzene, most of the reported data in the literature are on the sublimation curve. The summary for the experimental data is given in Table 7, and the results are shown from Figure 6 to Figure 11. Benzene properties obtained via simulations are summarized in Table S1. Only the data that were selected for regression are exhibited in the figures (this also applies to the latter sections) because the outliers result in significantly large deviations.

Table 7. Summary for the experimental data and the corresponding fitted results (root-mean square (RMS) deviations and absolute average relative deviations (AAD)) along the sublimation curve. The subscript “all” refers to all the reported data in the literature, and “tuned” refers to the data that were fitted in this work.

Property	Source	Year	T/K	N_{all}	N_{tuned}	$\text{RMS}_{\text{all}}/\%$	$\text{AAD}_{\text{all}}/\%$	$\text{RMS}_{\text{tuned}}/\%$	$\text{AAD}_{\text{tuned}}/\%$
V_m	Andrew and Eades ⁵⁷	1953	78.2, 270.2	2	0	0.67	0.58	-	-
	Andrews and Ubbelohde ⁵⁸	1955	278.7	1	1	0.17	0.17	0.17	0.17
	Bacon et al. ⁵⁹	1964	138, 218	2	2	0.79	0.78	0.79	0.78
	Biltz et al. ⁶⁰	1930	90.2, 194.2	2	2	0.14	0.12	0.14	0.12
	Cox and Bragg ⁶¹	1932	251	1	0	2.87	2.87	-	-
	Cox et al. ⁶²	1958	270.2	1	1	0.58	0.58	0.58	0.58
	Craven et al. ⁶³	1993	4.9-278.6	15	15	0.52	0.51	0.52	0.51
	Dunitz and Ibberson ⁵²	2008	5.5-274	15	15	0.23	0.18	0.23	0.18
	Ferche ⁶⁴	1891	278.5	1	0	0.79	0.79	-	-
	Fortes and Capelli ⁵³	2018	10-275	12	12	0.19	0.16	0.19	0.16
	Heuse ⁶⁵	1930	20	1	1	0.76	0.76	0.76	0.76
Heydweiller ⁶⁶	1897	270.2-276.6	8						

	Andrews et al. ⁷¹	1926	255.2-278.5	4	0	10.19	8.85	-	-
	Brucksch and Ziegler ⁷²	1942	15-270	28	28	1.63	1.48	1.63	1.48
	Dewar ⁷³	1913	50	1	1	4.47	4.47	4.47	4.47
	Diedrich ⁷⁴	2005	180.2-270.2	19	0	4.23	3.95	-	-
	Hahnenkamp ⁷⁵	2008	190-270	17	17	0.87	0.74	0.87	0.74
	Huffman et al. ⁷⁶	1930	92.6-259.5	16	16	1.62	1.56	1.62	1.56
	Maass and Waldbauer ⁷⁷	1925	93.2-273.2	10	0	7.30	6.49	-	-
	Nan ^{78a}	2004	78.4-265.0	55	55	1.06	0.85	1.06	0.85
	Nernst ⁷⁹	1911	24.4-200.9	12	12	5.90	4.67	5.90	4.67
	Oliver et al. ⁸⁰	1948	13-278.6	92	92	3.72	2.51	3.72	2.51
	Stull ^{81b}	1937	90-270	19	19	1.73	1.62	1.73	1.62
	Craven et al. ^{82a}	1993	19.0-285.5	12	9	19.19	13.61	8.69	6.81
	Ferche ⁶⁴	1891	275.2	1	0	23.19	23.19	-	-
	Fortes and Capelli ^{53a}	2018	18.3-263.0	11	11	7.47	6.55	7.47	6.55
K_S	Brunel ⁸³	1979	270	1	1	4.22	4.22	4.22	4.22
	Heseltine et al. ⁸⁴	1964	170-250	9	9	1.23	0.92	1.23	0.92
	Růžička et al. ⁸⁵	2014	150-270	13	13	1.18	1.00	1.18	1.00
p_{sub}^c	Barker ⁸⁶	1910	195.7	1	0	24.75	24.75	-	-
	Choi and Brown ⁸⁷	1966	227.7-273.2	4	3	1.50	1.25	0.92	0.82

De Kruif and Van Ginkel ⁸⁸	1977	183.0-197.0	10	0	2.23	1.76	-	-
De Kruif ⁸⁹	1980	183.4-196.7	10	0	1.02	0.81	-	-
Deitz ⁹⁰	1933	184.3-200.2	4	2	5.01	3.74	1.09	0.93
Ferche ⁶⁴	1891	272.3-278.5	30	26	4.86	2.37	1.14	0.77
Ha et al. ⁹¹	1976	228.7-273.2	14	14	0.89	0.70	0.89	0.70
Jackowski ⁹²	1974	220.8-278.7	21	14	3.71	2.41	1.17	0.89
Kiss ⁹³	1972	234.3-277.2	17	15	1.47	1.03	0.76	0.67
Liu and Dickhut ⁹⁴	1994	257.8-268.2	2	0	15.76	14.04	-	-
Milazzo ⁹⁵	1956	195.2-273.1	10	10	1.16	0.84	1.16	0.84
Milazzo ⁹⁶	1956	195.2-257.2	6	6	1.18	1.11	1.18	1.11
Miljevic et al. ⁹⁷	1977	202.1-278.5	39	35	1.42	0.82	0.63	0.52
Mündel ⁹⁸	1913	214.6-238.1	7	0	9.47	9.35	-	-
Radulescu and Alexa ⁹⁹	1938	273.2-277.2	3	2	8.01	5.71	1.97	1.76
Rastogi et al. ¹⁰⁰	1967	260.2-273.2	5	0	20.56	19.57	-	-
Růžička et al. ⁸⁵	2014	233.2-260.7	36	36	0.25	0.22	0.25	0.22
Young ¹⁰¹	1910	263.2-273.2	2	0	24.06	22.52	-	-

a) Data were read from a plot and were assigned half of the weighting factor. b) The apparatus was calibrated based on the data reported by Huffman et al.⁷⁶ c) the fitting for sublimation was calculated as $\frac{G_{fluid} - G_{solid}}{RT}$ using experimental (T, p) as inputs, and the results are exhibited in the form of pressure in Figure 11. Here for the i^{th} point, G_{fluid} refers to the Gibbs energy from the fluid model, G_{solid} is the fitted Gibbs energy from the solid EOS.

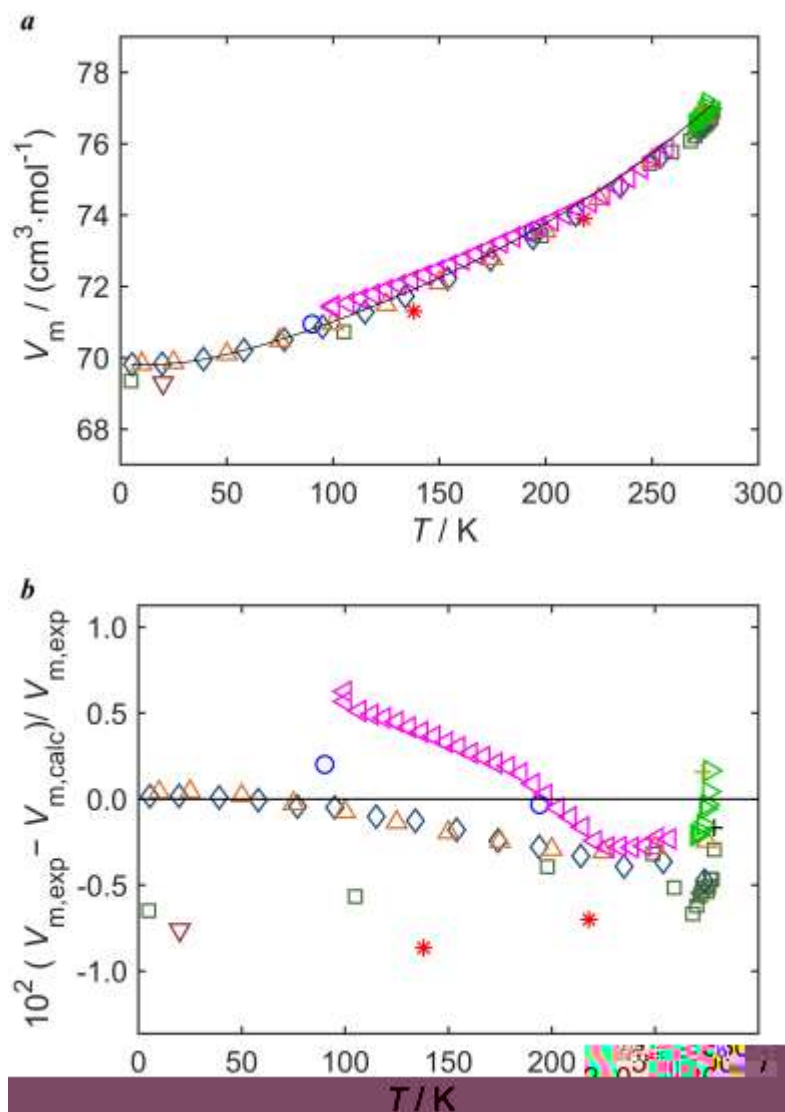


Figure 6. Comparison between the molar volume data, V_m , along the sublimation curve and the equation of state fit as a function of temperature. **a.** V_m measurements and model calculations (black curve); **b.** fractional deviations from the experimental data. Legend: + Andrews and Ubbelohde;⁵⁸ * Bacon et al.;⁵⁹ ○ Biltz et al.;⁶⁰ × Cox and Smith;¹⁰² □ Craven et al.;⁶³ ◇ Dunitz and Ibberson;⁵² △ Fortes and Capelli;⁵³ ▽ Heuse;⁶⁵ ▹ Heydweiller;⁶⁶ ◊ McConville et al.;⁶⁸ + Ziegler and Ditzel.⁶⁹

Figure 6 exhibits the literature molar volume data along the sublimation curve. Experimental methods include neutron and X-ray diffraction. It can be observed that the data from Craven et al.,⁶³ Dunitz and Ibberson,⁵² Fortes and Capelli,⁵³ Heydweiller⁶⁶ and McConville et al.⁶⁸ deviate by up to 0.5% from the model at a given temperature, and contribute to most of the deviations in the plot. These data sources were kept in the regression process, as only outliers that deviate from the other data points by more than

1% were excluded. Biltz et al.⁶⁰ reported the uncertainty of measurement is around 0.3%, while uncertainties were not reported for most of the literature data. The equation of state matches the molar volume from Dunitz and Ibberson⁵² and Fortes and Capelli⁵³ well. Overall, good agreement has been achieved for the molar volume data along the sublimation curve, well within the consistency of different experimental data sets.

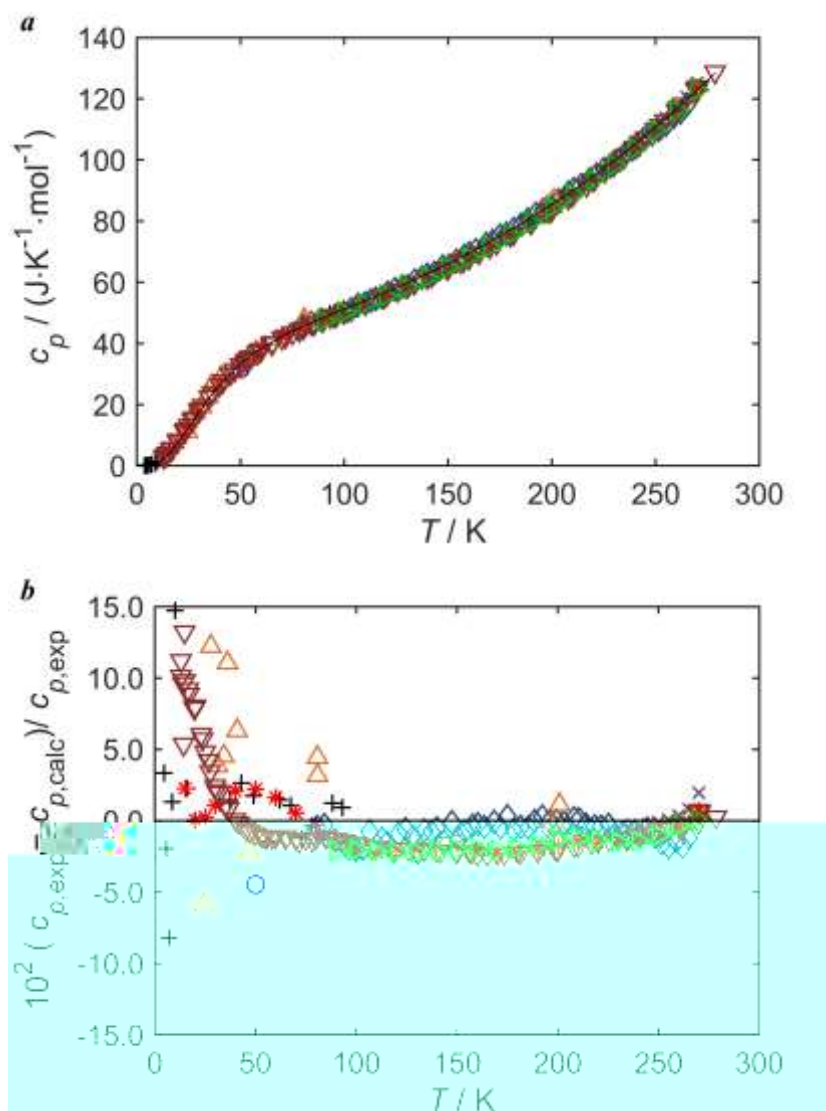


Figure 7. Comparison between the isobaric heat capacity data, c_p , along the sublimation curve and the equation of state fit as a function of temperature. **a.** c_p measurements and model calculations (black curve); **b.** fractional deviations from the experimental data. Legend: + Ahlberg et al.;⁷⁰ * Brucksch and Ziegler;⁷² ○ Dewar;⁷³ × Hahnenkamp;⁷⁵ □ Huffman et al.;⁷⁶ ◇ Nan;⁷⁸ △ Nernst;⁷⁹ ▽ Oliver et al.;⁸⁰ ▷ Stull.⁸¹

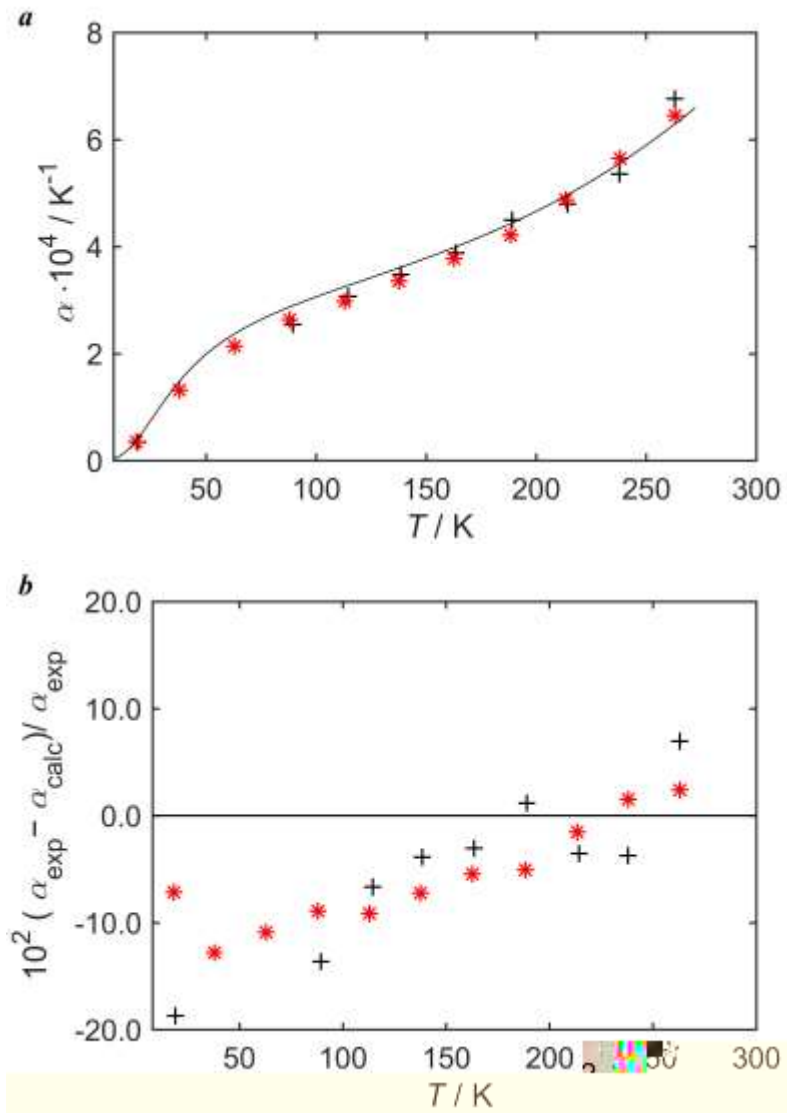


Figure 8. Comparison between the thermal expansivity data, α , along the sublimation curve and the equation of state fit as a function of temperature. **a.** measurements and model calculations (in a black curve); **b.** fractional deviations from the experimental data. Legend: + Craven et al.;⁸² * Fortes and Capelli.⁵³

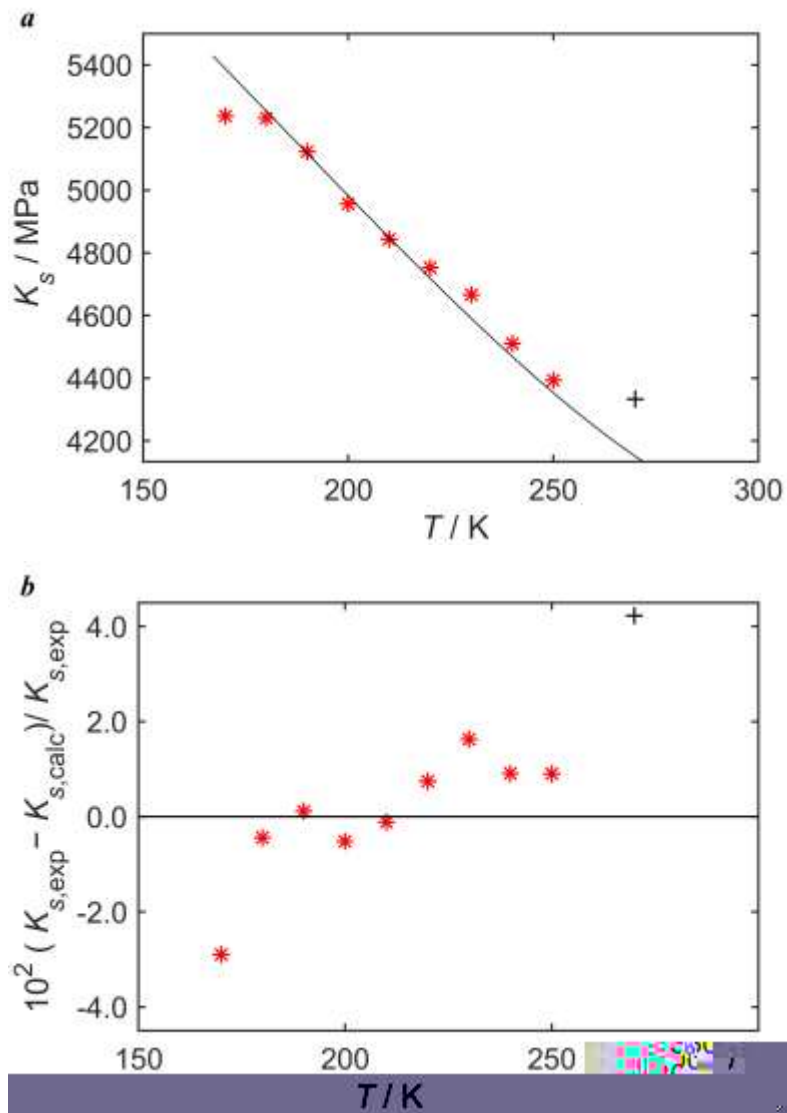


Figure 9. Comparison between the isentropic bulk modulus data, K_s , along the sublimation curve and the equation of state fit as a function of temperature. *a*. K_s measurements and model calculations (in a black curve); *b*. fractional deviations from the experimental data. Legend: + Brunel;⁸³ * Heseltine et al.⁸⁴

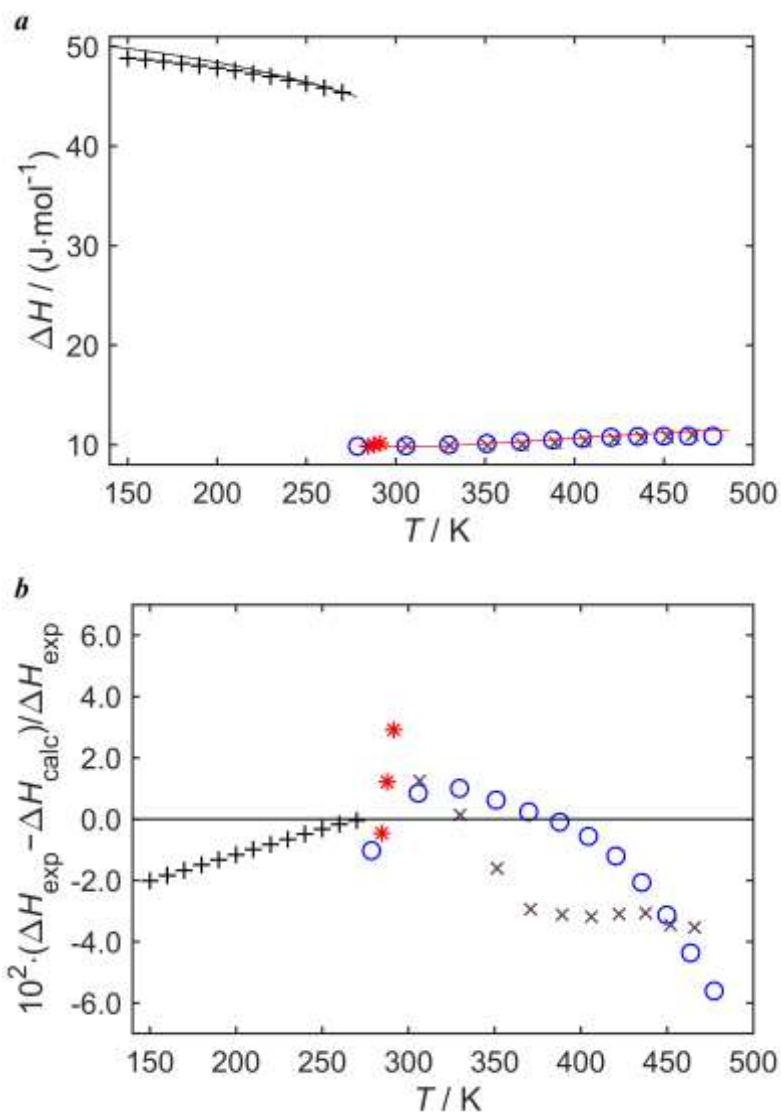


Figure 10. Comparison between the enthalpy of sublimation (melting) data, ΔH , and the equation of state description as a function of temperature. **a.** enthalpy measurements and model calculations (black curve for sublimation and red curve for melting); **b.** fractional deviations from the experimental data. Legend for enthalpy of sublimation: + Růžička et al.⁸⁵ Legend for enthalpy of melting: * Azreg-Aïnou;^{103, 104} ○ Bridgman;¹⁰⁵ × Xu et al.¹⁰⁶

In Figure 7 it can be observed that the deviations for isobaric heat capacity at low temperatures are less than 10% for most points, and at $T > 50$ K almost all the c_p data can be described within 2.5%. Although most data do not include such estimates, Huffman et al.⁷⁶ stated the uncertainty of their reported heat capacities, determined via an aneroid calorimeter, should be less than 1%. In the low temperature region, it is difficult to tune to the experimental values within a few percent because the reported values are very small (less than $10 \text{ J}\cdot\text{K}^{-1}\cdot\text{mol}^{-1}$), and data from different sources are

inconsistent at the level of (1 to 3) $\text{J}\cdot\text{K}^{-1}\cdot\text{mol}^{-1}$. One datum at 3.8 K from Ahlberg et al.⁷⁰ exhibits a deviation of -30.6% from the model and for clarity is not exhibited in Figure 7.

Figure 8 shows how the thermal expansivities calculated with the tuned model follow the data's trend with temperature and can describe most of the points within 10%. The two worst cases of 14% and 19% are at (89 and 19) K, respectively. The reported values from Craven et al.⁸² and Fortes and Capelli⁵³ differ by between (5 to 12)% at a given temperature. It seems that thermal expansivity is relatively hard to regress well; for solid CO_2 the AAD in this property is 11.7%.²³ The deviations calculated for benzene's thermal expansivity exhibited a trend with parameter adjustment that was contradictory to those for enthalpy, sublimation, and isentropic bulk modulus. As a result, thermal expansivity calculations were allowed to deviate more systematically at temperatures below 150 K to enable a good representation of the other properties.

Figure 9 exhibits the isentropic bulk modulus along the sublimation curve, which were obtained via elastic constants measured by Brillouin scattering⁸³ and from speed of sound measurements.⁸⁴ The inclusion of the cold curve parameters c_1 to c_3 in the model

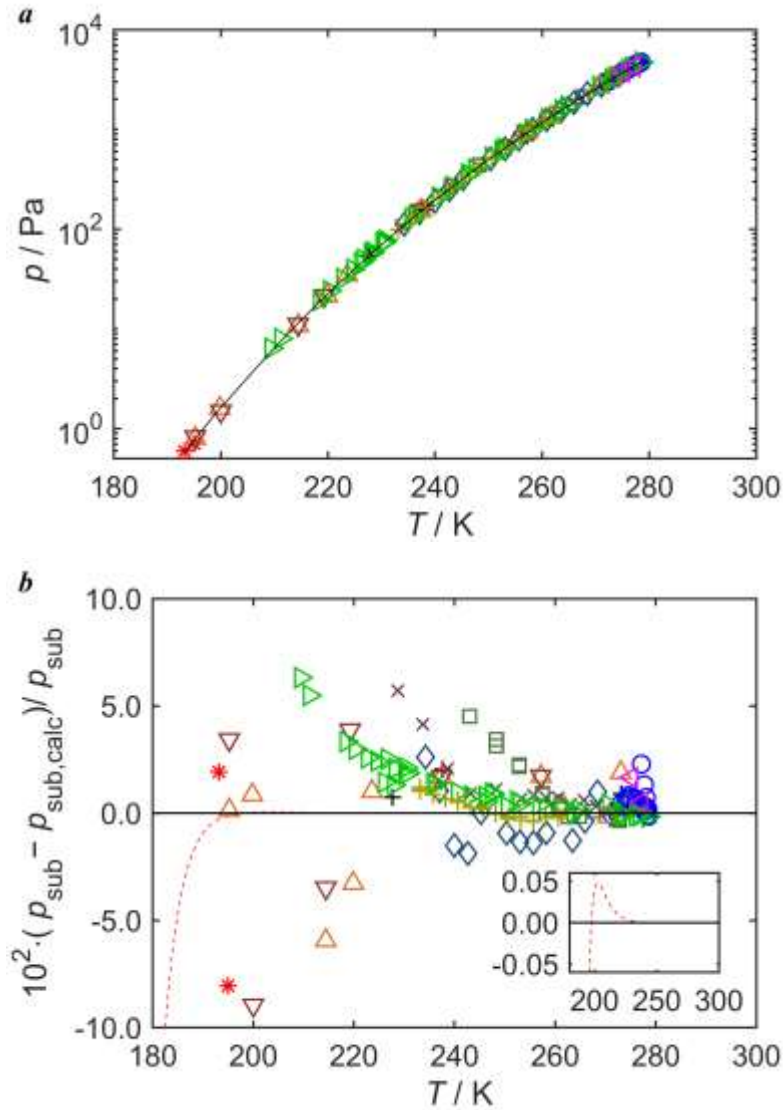


Figure 11. Comparison between the sublimation pressure measurements, p_{sub} , and the equation of state fit as a function of temperature. **a.** sublimation pressure measurements and model calculations (in a black curve) on a logarithmic vertical scale; **b.** fractional deviations from the experimental data. Legend: + Choi and Brown;⁸⁷ * Deitz;⁹⁰ ○ Ferche;⁶⁴ × Ha et al.;⁹¹ □ Jackowski;⁹² ◇ Kiss;⁹³ △ Milazzo;⁹⁵ ▽ Milazzo;⁹⁶ ▹ Miljevic et al.;⁹⁷ ▹ Radulescu and Alexa;⁹⁹ + Růžička et al.⁸⁵ red dashed curve in the main plot and the inset: auxiliary function. The triple point is (278.67 K, 4780 Pa).

To calculate a sublimation pressure, a solid-vapor phase equilibrium state must be identified where the difference between the molar Gibbs free energy of the solid and fluid phases vanishes. In this work, p_{sub} was determined by finding the condition where the G_m value calculated with the new fundamental equation of state equaled that

determined with the extrapolated reference EOS for the fluid. Růžička et al.⁸⁵ used static method with a STAT6 apparatus to measure the vapor pressure with an uncertainty around 0.5%. The solid EOS can describe the majority of the experimental sublimation pressures within a deviation of 5%, with only six points excepted. At temperatures below 220 K, the data from Milazzo,⁹⁵ Milazzo⁹⁶ and Miljevic et al.⁹⁷ differ from the calculated sublimation pressures by up to 10%; the small pressure values in this low temperature region are more difficult to fit with small relative differences. The auxiliary function matches the EOS calculations very well, with exceptions at temperatures below 195 K where no data exist.

6.2. Data on the Melting Curve

A data summary for the measurements performed along the melting curve is presented in Table 8 and shown in Figure 12. Melting data achieved via computation are listed in Table S1. Results for the enthalpy of fusion were presented in Figure 10 and are not discussed further in this subsection.

Table 8. Summary for the experimental data and the corresponding fitted results (root-mean square (RMS) deviations and absolute average relative deviations (AAD)) along the melting curve. The subscript “all” refers to all the reported data in the literature, and “tuned” refers to the data that were fitted in this work.

Property	Source	Year	T/K	N_{all}	N_{tuned}	$\text{RMS}_{\text{all}}/\%$	$\text{AAD}_{\text{all}}/\%$	$\text{RMS}_{\text{tuned}}/\%$	$\text{AAD}_{\text{tuned}}/\%$
	Azreg-Aïnou ^{103, 104a}	2006	284.6-306.7	10	3	5.01	4.48	1.84	1.53
	Bridgman ¹⁰⁵	1914	278.6-477.4	12	12	2.41	1.73	2.41	1.73
	Osugi et al. ¹¹⁰	1965	288.2-298.2	3	0	8.80	8.44	-	-
	Xu et al. ¹⁰⁶	2007	306.4-466	10	10	2.76	2.54	2.76	2.54
$\rho_{\text{melt}}^{\text{b}}$	Azreg-Aïnou ^{103, 104}	2006	284.6-306.7	10	10	0.68	0.59	0.68	0.59
	Block ^{111, 112c}	1913	298.2-324.2	5	5	0.10	0.09	0.10	0.09
	Bridgman ¹⁰⁵	1914	305.7-463.7	10	0	0.50	0.43	-	-
	Bridgman ¹¹³	1949	297.2	1	1	0.24	0.24	0.24	0.24
	Deffet ¹¹⁴	1935	283.2-305.2	6	6	0.52	0.31	0.52	0.31
	Deffet ¹¹⁵	1942	293.1-300.6	2	2	0.13	0.11	0.13	0.11
	Domanska and Morawski ¹¹⁶	2005	293.2-353.2	7	7	0.16	0.14	0.16	0.14
	Domanska and Morawski ¹¹⁷	2007	328.2-363.2	8	8	0.16	0.15	0.16	0.15
	Easteal et al. ¹¹⁸	1985	281.3-310.3	12	10	1.07	0.54	0.25	0.17
	Figuière et al. ¹¹⁹	1978	298.2-324.2	6	6	0.25	0.23	0.25	0.23
	Fruhling ¹²⁰	1951	306.5-331.2	2	2	0.32	0.32	0.32	0.32
	Ghelfenstein and Szwarc ¹²¹	1975	298.2-324.2	3	3	0.11	0.11	0.11	0.11
	Hulett ¹²²	1899	279.2-290.7	22	12	55.35	12.88	0.34	0.27

Makita and Takagi ¹²³	1968	283.2-323.2	7	6	0.51	0.30	0.14	0.13
Nagaoka ¹²⁴	1987	283.2-323.2	7	7	0.45	0.33	0.45	0.33
Osugi ¹²⁵	1968	288.2-298.2	4	1	1.51	1.26	0.43	0.43
Pruzan ¹²⁶	1976	301.7-324.2	2	2	0.36	0.32	0.36	0.32
Pruzan ¹²⁷	1979	302-325	2	2	0.52	0.49	0.52	0.49
Sun et al. ¹²⁸	1987	279.6-323.1	11	8	1.69	0.89	0.13	0.10
Tanaka and Kawakami ¹²⁹	1996	278.8-323.2	10	8	36.93	12.1	0.61	0.50
Xu et al. ¹⁰⁶	2007	306.4-466.0	10	0	0.52	0.44	-	-
Yokoyama et al. ¹³⁰	1993	294.7-329.8	8	4	0.46	0.40	0.46	0.40

a) Data were obtained from fitted correlations. b) the fitting for melting was calculated as $\frac{G_{fluid} - G_{solid}}{RT}$ using experimental (T, p) as inputs, and the results are exhibited in the form of pressure in Figure 12. Here for the i^{th} point, G_{fluid}^i refers to the Gibbs energy from the fluid model, G_{solid}^i is the fitted Gibbs energy from the solid EOS. c) Data were obtained from Table 1 of Figuière et al.¹¹⁹

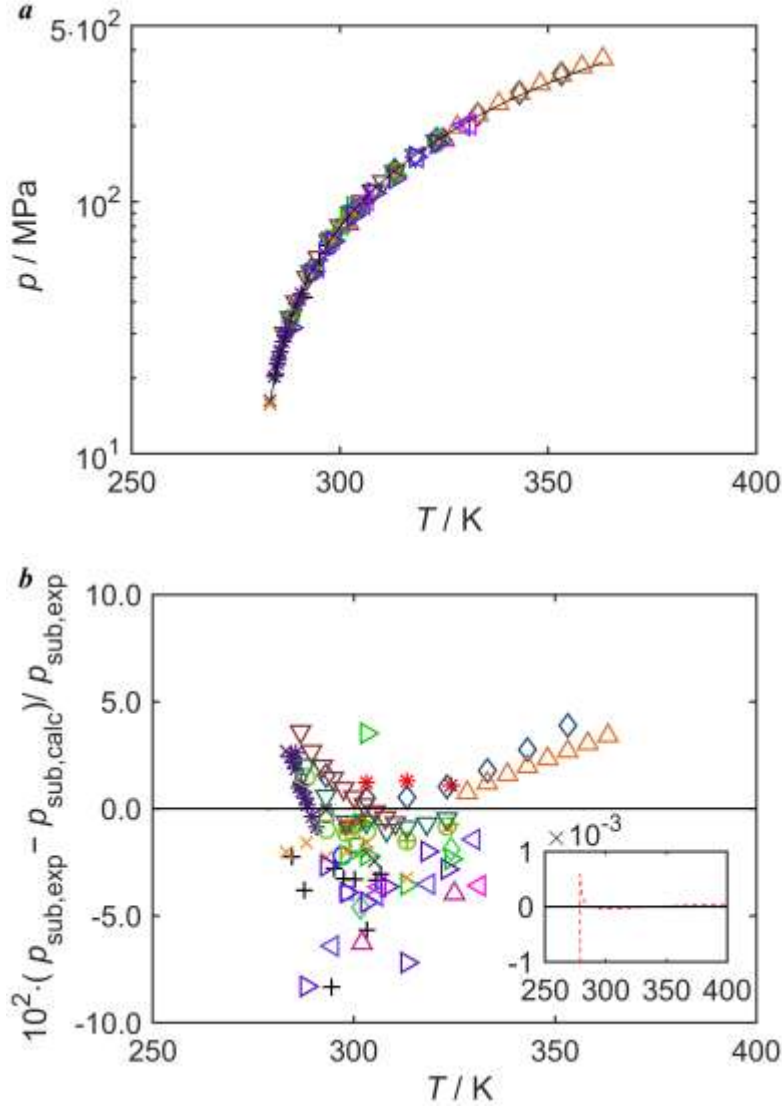


Figure 12. Comparison between the melting pressure measurements, p_{melt} , and the equation of state fit as a function of temperature. **a.** p_{melt} measurements and model calculations (in a black curve); **b.** fractional deviations from the experimental data. Legend: + Azreg-Aïnou,^{103, 104} * Block;^{111, 112} ○ Bridgman;¹¹³ × Deffet;¹¹⁴ □ Deffet;¹¹⁵ ◇ Domanska and Morawski;¹¹⁶ △ Domanska and Morawski;¹¹⁷ ▽ Easteal et al.;¹¹⁸ ▷ Figuière et al.¹¹⁹; ◁ Fruhling;¹²⁰ + Ghelfenstein and Szwarc;¹²¹ * Hulett;¹²² ○ Makita and Takagi;¹²³ × Nagaoka;¹²⁴ □ Osugi;¹²⁵ ◇ Pruzan;¹²⁶ △ Pruzan;¹²⁷ ▽ Sun et al.;¹²⁸ ▷ Tanaka and Kawakami;¹²⁹ ◁ Yokoyama et al.;¹³⁰ red dashed curve in the main plot and the inset: auxiliary function. The triple point is (278.67 K, 0.00478 MPa).

Similar to the sublimation pressure, p_{melt} was calculated by estimating an equality of the Gibbs free energies calculated with the solid EOS developed in this work and the reference EOS for fluid benzene. The majority of the melting point data are represented within 5%, with only a few exceptions located mostly near the triple point. In this region the measurements have relatively large uncertainties (e.g. for Azreg-Aïnou,^{103, 104}

$u_r(p_{\text{melt}}, 284.6 \text{ K}) = 5.8\%$ and $u_r(p_{\text{melt}}, 306.7 \text{ K}) = 1.2\%$). At a given temperature, the reported pressures from various sources differ systematically by up to 10%, particularly those measured around 300 K. However, it is unclear which data set is more accurate and thus all were retained in this work. The auxiliary function behaves nearly identical to the solid EOS: in the main figure of subplot *b* the red dashed curve vanishes near the zero line.

6.3. Single-phase Data Measured at High Pressure

Single-phase data at high pressures are listed in Table 9 and shown in Figure 13 and Figure 14. Simulation results in the literature are summarized in Table S2. Some of the measurements reported by the authors include data for other solid phases of benzene (e.g. solid phase II); these are not included here.

Table 9. Summary of the experimental data and the corresponding fitted results (root-mean square (RMS) deviations and absolute average relative deviations (AAD)) for single-phase data measured at high pressures. The subscript “all” refers to all the reported data in the literature, and “tuned” refers to the data that were fitted in this work.

Property	Source	Year	T/K	p/MPa	N_{all}	N_{tuned}	$RMS_{all}/\%$	$AAD_{all}/\%$	$RMS_{tuned}/\%$	$AAD_{tuned}/\%$
V_m	Budzianowski and Andrzej ¹³¹	2005	296	300-1100	3	2	2.88	2.00	0.54	0.53
	Figuière et al. ^{119a,b}	1978	253.2-324.2	0-490	114	114	1.47	1.41	1.47	1.41
	Hofmann and Kuleshova ¹³²	2014	138-270	100	4	0	2.89	2.55	-	-
	Katrusiak et al. ^{51b}	2010	295	79.5-1287.9	40	40	0.63	0.48	0.63	0.54
V_m^c	Bridgman ¹³³	1941	323.2	490-981	2	0	8.41	8.41	-	-
	Bridgman ¹³⁴	1942	298.2-348.2	490-981	4	0	10.80	9.16	-	-
	Bridgman ¹¹³	1949	297.2	245-981	3	0	0.33	0.33	-	-
$c_{p,m}$	Ross et al. ¹³⁵	1979	300	206.6-1600	7	0	5.77	5.10	-	-
	Fuchs et al. ¹³⁶	1979	253.6-355.2	0.4-411.1	164	155	15.20	6.70	4.85	4.15
	Pruzan et al. ¹²⁷	1979	302-325	113-657	31	31	5.28	4.36	5.28	4.36
	Pruzan et al. ¹³⁷	1986	268-355	16-423.5	40	0	20.69	16.52	-	-

a) Data were read from a plot and were assigned half of the weighting factor. b) Data were obtained from fitted correlations. c) it refers to the volume decrement upon compression at a given temperature.

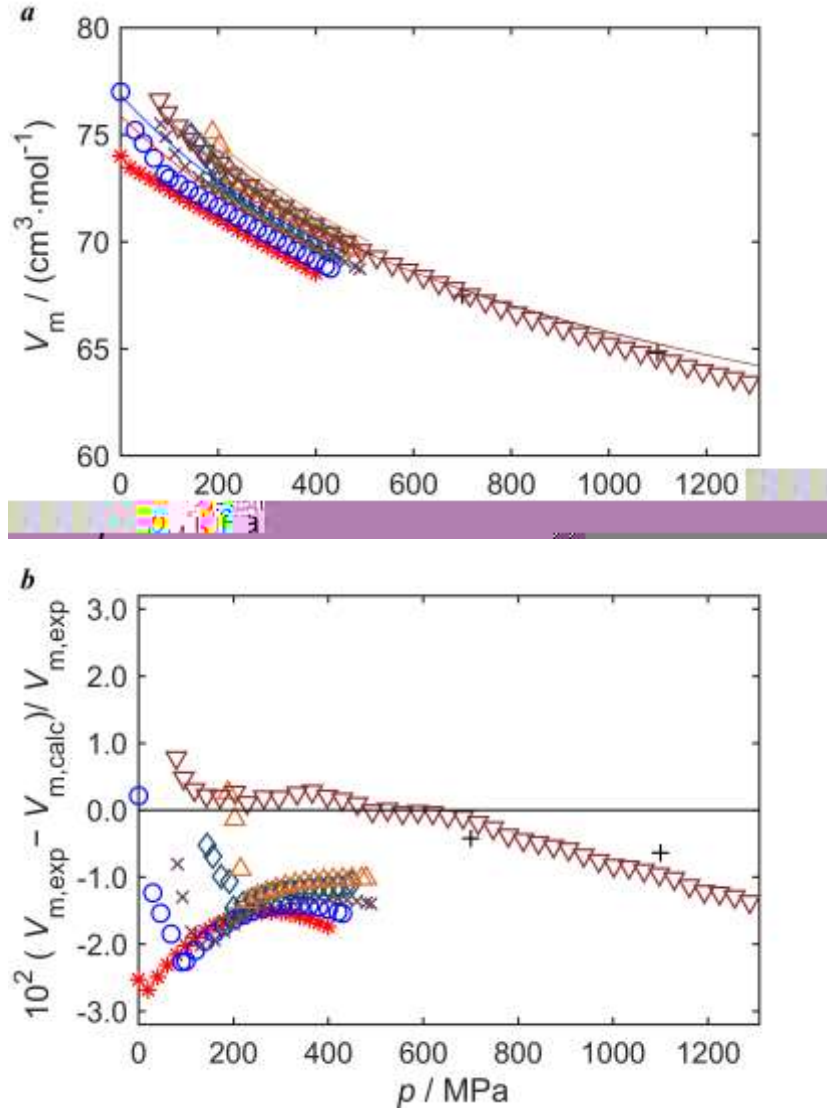


Figure 13. Comparison between the molar volume data V_m measured for the solid phase at high pressures and the equation of state fit as a function of pressure. **a**. V_m measurements and model calculations; **b**. fractional deviations from the experimental data. Legend: + Budzianowski and Andrzej¹³¹ (296.00 K); * Figuière et al.¹¹⁹ (253.15 K); O Figuière et al.¹¹⁹ (273.15 K); X Figuière et al.¹¹⁹ (298.15 K); □ Figuière et al.¹¹⁹ (301.65 K); ◇ Figuière et al.¹¹⁹ (313.15 K); △ Figuière et al.¹¹⁹ (324.15 K); ▽ Katrusiak et al.⁵¹ (295.00 K). The model descriptions for different data sets are given in the corresponding colored curves.

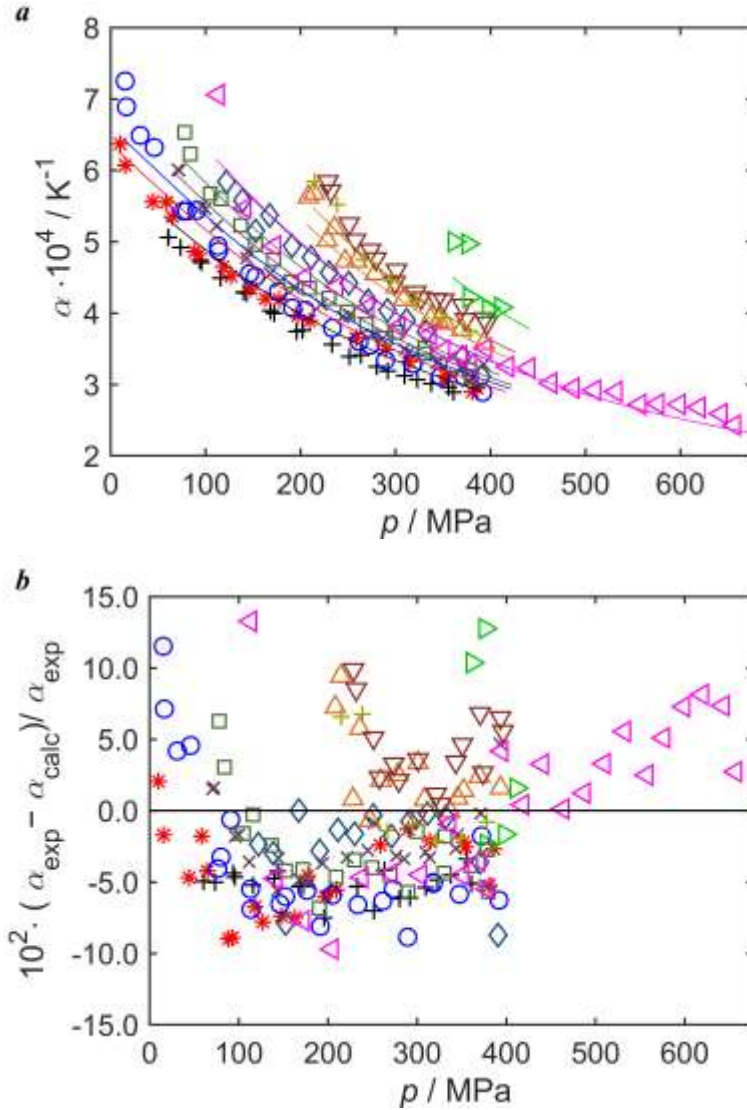


Figure 14. Comparison between the thermal expansivity data, α , measured for the solid phase at high pressure and the equation of state fit as a function of pressure. **a.** measurements and model calculations; **b.** fractional deviations from the experimental data. Legend: + Fuchs et al.¹³⁶ (253.60 K); * Fuchs et al.¹³⁶ (265.00 K); \circ Fuchs et al.¹³⁶ (272.40 K); \times Fuchs et al.¹³⁶ (278.80 K); \square Fuchs et al.¹³⁶ (287.80 K); \diamond Fuchs et al.¹³⁶ (301.40 K); \triangle Fuchs et al.¹³⁶ (314.20 K); ∇ Fuchs et al.¹³⁶ (324.70 K); \triangleright Fuchs et al.¹³⁶ (355.16 K); \blacktriangleleft Pruzan et al.¹²⁷ (302.00 K); + Pruzan et al.¹²⁷ (325.00 K).

Figure 13 compares the experimental molar volume at high pressures with the equation of state. The differences are within 2.5% for all the data with very few exceptions. The reported V_m from Figuière et al.¹¹⁹ were either read from a plot or calculated via a correlation that was fitted to the experimental data. Thus, they are not of the same quality as the molar volumes reported along the sublimation curve. Experimental

methods include X-ray diffraction (Budzianowski and Andrzej,¹³¹ Hofmann and Kuleshova,¹³² and Katrusiak et al.⁵¹), slyphon method (Figuière et al.¹¹⁹) and neutron scattering (Hofmann and Kuleshova¹³²).

For high pressure thermal expansivity, both Fuchs et al.¹³⁶ and Pruzan et al.¹²⁷ used the piezothermal method for their calorimetric measurements. In Figure 14, the data have deviations from the model of less than 10%. At 302 and 325 K, the two literature sources are inconsistent by 10%. It is not clear which data set should be given with primary consideration, and this model produces a compromise of the reported values.

7. Uncertainty and Physical Behavior Examination

The resulting EOS is able to describe all thermodynamic properties of solid benzene at temperatures up to 470 K and at pressures up to 1800 MPa. Based on comparisons with the experimental data, the estimated relative uncertainties for molar volume are 0.2% on the sublimation curve increasing to 1.5% in the compressed solid. For isobaric heat capacity on the sublimation curve, the uncertainties are 8% for $T < 20$ K, 4% for $20 < T < 50$, and 1% for $T > 50$ K. The uncertainties for other calculated properties are estimated to be 4% for thermal expansivity; 1% for isentropic bulk modulus; 1% for enthalpy of sublimation and melting; and 2% and 3%, respectively for the computed sublimation and melting pressures. For the heat capacity of the compressed solid, the data from Ross¹³⁵ at 300 K were read from a plot and stated to have a relative uncertainty of 10%. They were not included in the tuning process and deviate from the optimised model with a relative RMS deviation of 5.8%. The solid model's description of sublimation and melting enthalpies as well as the solid-fluid equilibrium conditions have an uncertainty that includes the extrapolation of the reference fluid EOS. The accuracy of these extrapolated fluid values is difficult to quantify because there are no experimental data for comparison.

It is important to examine whether the model's behavior is physical within the range of validity for this equation of state at conditions where no data exists. This helps ensure the model's predictions are reasonable when it is used at conditions beyond those incorporated by the regression. Figure 15 shows the pressure, isentropic bulk modulus, isobaric expansivity, and thermal pressure coefficient calculated for several isotherms and at saturated conditions. Similar to the results for solid CO₂,²³ the pressure isotherms become parallel in the low molar volume region. The isentropic bulk modulus does not vary much with temperature but is dependent on the molar volume, decreasing sharply at conditions away from the triple point. The isobaric expansivity increases rapidly from 0 to 200 K (at 0 K it is zero), while above 200 K it becomes insensitive to temperature. The thermal pressure coefficient — exhibits a similar dependence on temperature. At the triple point, the isentropic bulk modulus and thermal expansivity reach a minimum and maximum, respectively. In the physical property plots, the highest temperature is 450 K instead of 470 K because the latter isotherm is very close

to the triple point (solid I-solid II-fluid) temperature and remains in the solid phase for a relatively small range of molar volumes.

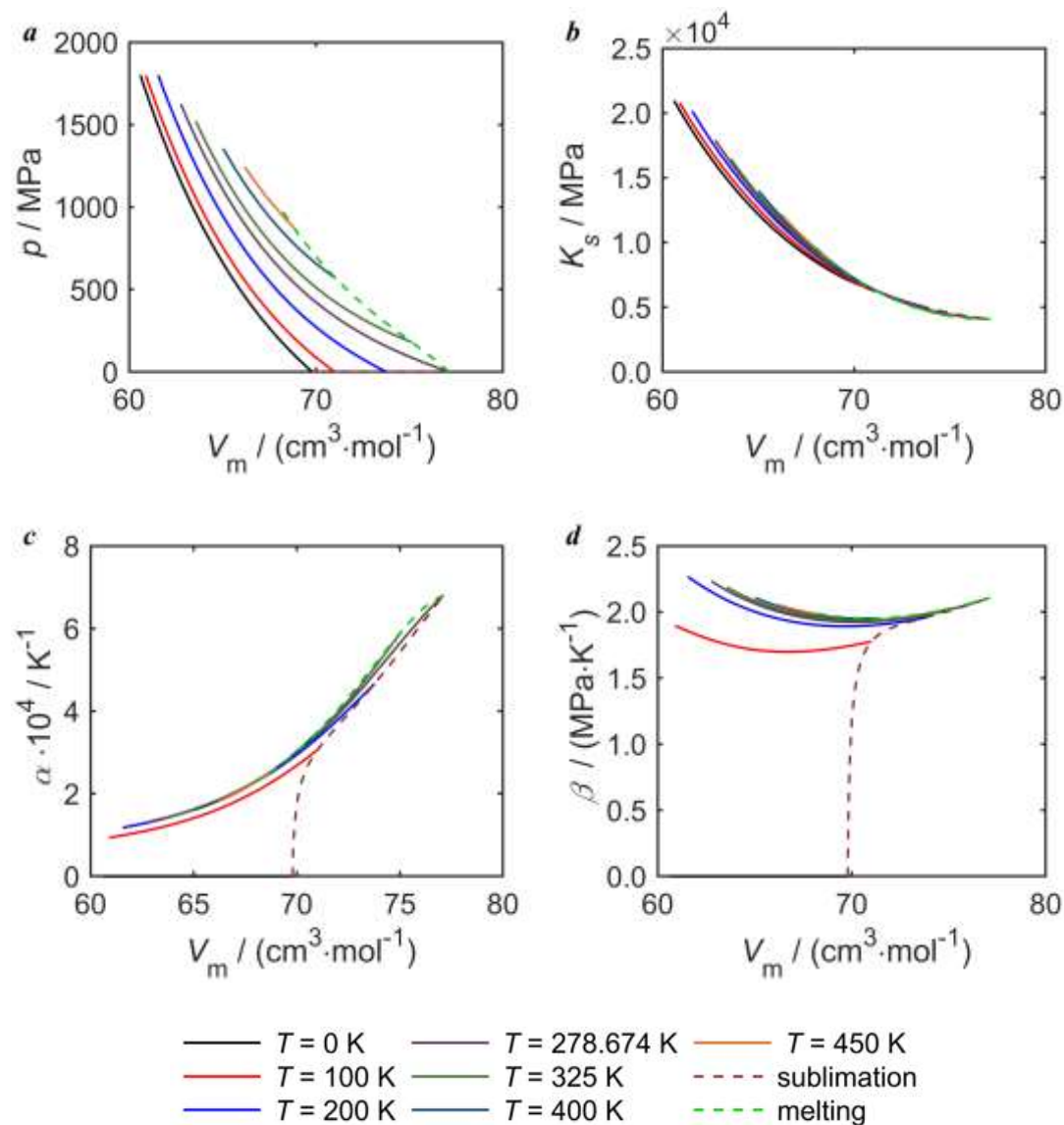


Figure 15. Thermodynamic properties calculated from the equation of state to examine the thermodynamic surface behavior. **a.** p - V_m curves; **b.** isentropic bulk modulus K_s ; **c.** isobaric expansivity ; **d.** thermal pressure coefficient .

Figure 16 exhibits the solid molar heat capacities calculated as a function of temperature along the saturation curves. The lattice heat capacity, determined from $c_{v,m} - c_{\text{int}}$, reaches a limit of $6.7R$ at temperatures above 300 K. At 470 K, the contribution of the internal

modes bring $c_{v,m}$ and $c_{p,m}$ to $18R$ and $20R$, respectively. The isobaric heat capacity increases appreciably as the temperature approaches the triple point condition where the solid is in its most expanded state.

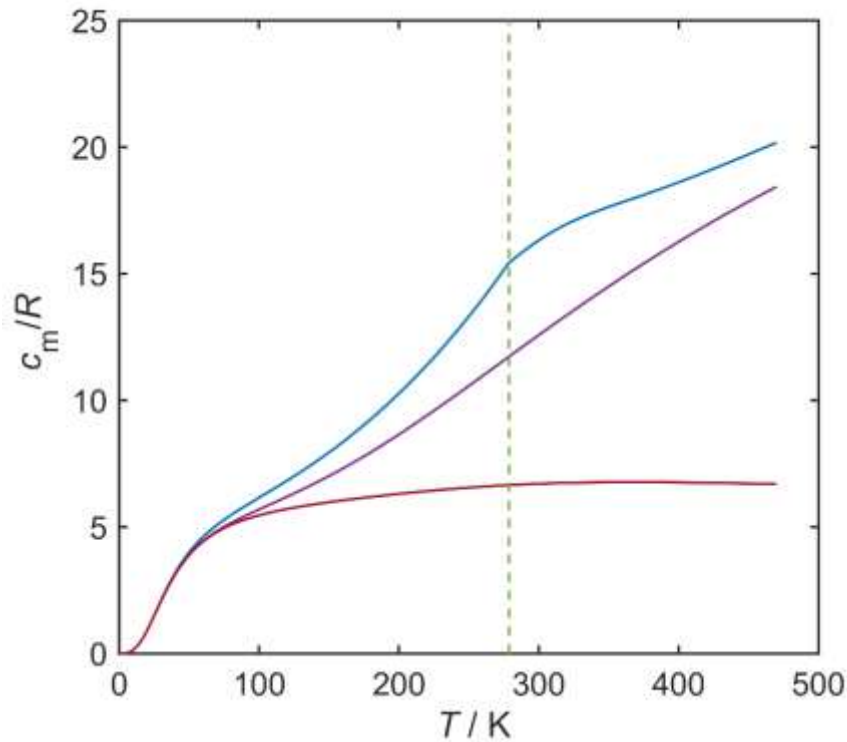


Figure 16. Molar heat capacities C_m as functions of temperature along the saturation (sublimation and melting) curve. Curves: dark red: lattice heat capacity $(c_{v,m}-c_{int})/R$; purple: isochoric heat capacity $c_{v,m}/R$; dark blue: isobaric heat capacity $c_{p,m}/R$. Vertical dashed line: triple point temperature.

The Grüneisen parameters are weakly dependent on the molar volume except at 0 K. As shown in Figure 17, at temperatures above 100 K, γ hardly changes with molar volume and lies in a range between 1 and 2.5. In the global fit process, the Grüneisen parameter behavior at 0 K was constrained manually to ensure no obvious local maxima or minima occurred.

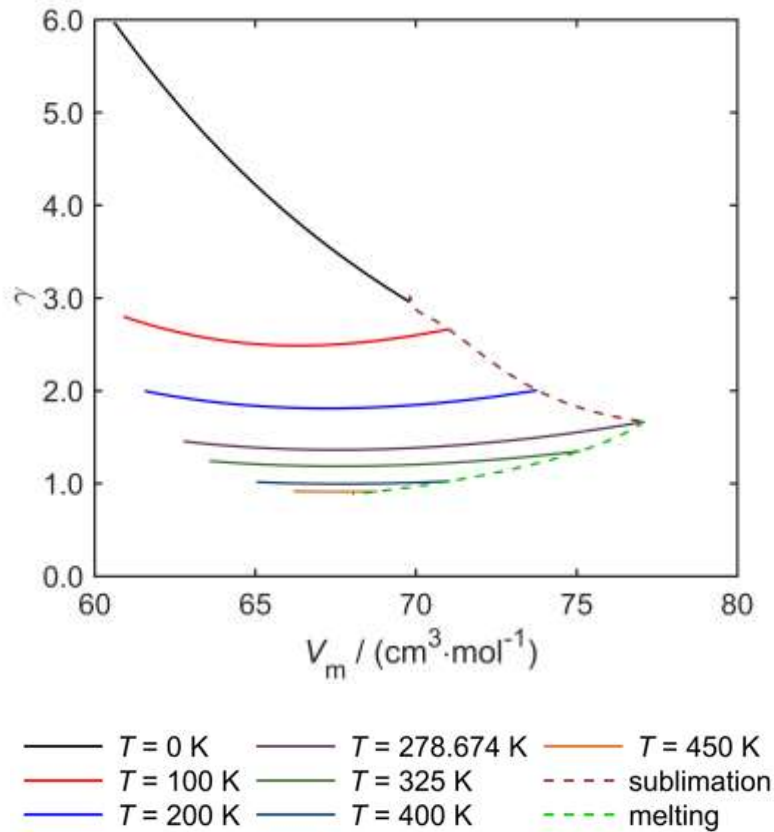


Figure 17. Grüneisen parameter curves for isotherms and saturated conditions as a function of molar volume.

8. Conclusions

For the first time, a reference Helmholtz equation of state for solid I benzene has been developed which can be used to calculate all thermodynamic properties. The EOS is physically based on the quasi-harmonic approximation and can be used for property calculations at temperatures up to 470 K and pressures up to 1800 MPa with confidence. It represents the available experimental data for solid benzene either within their experimental uncertainty or with a deviation similar to the scatter between data sets. New measurements of bulk modulus and heat capacity in the compressed solid would be useful, as there are currently no reliable data at any condition. New measurements of molar volume, thermal expansivity, and sublimation and melting equilibrium with lower uncertainties could provide insight into which data sets should be eliminated, as currently this equation of state strikes a balance in the systematic differences between

data from several authors. It may be possible to use the approach applied here to develop physically-based solid-phase EOS for industrial relevant compounds including toluene, cyclohexane and *p*-xylene.

9. Supplementary Information

There are two separate parts to the attached the Supplementary Information: (i) comparisons between this solid model and simulation-based literature data, and (ii) sample calculations made with this solid model, the extrapolated fluid EOS, and the auxiliary functions.

10. References

1. Y. A. Sataty, A. Ron and M. Brith, *Chem. Phys. Lett.* **23**, 500-503 (1973).
2. M. Podsiadło, K. Jakóbek and A. Katrusiak, *CrystEngComm* **12**, 2561-2567 (2010).
3. F. H. Ree, *J Chem Phys* **70**, 974-983 (1979).
4. L. Ciabini, M. Santoro, R. Bini and V. Schettino, *J Chem Phys* **115**, 3742-3749 (2001).
5. L. Morávková, Z. Wagner and J. Linek, *Fluid Phase Equilib.* **209**, 81-94 (2003).
6. R. D. Chirico and W. V. Steele, *Ind. Eng. Chem. Res.* **33**, 157-167 (1994).
7. R. Engelke, P. J. Hay, D. A. Kleier and W. R. Wadt, *J. Am. Chem. Soc.* **106**, 5439-5446 (1984).
8. R. Pucci and N. March, *J. Chem. Phys.* **74**, 1373-1378 (1981).
9. M. Thol, E. W. Lemmon and R. Span, *High Temp High Press* **41**, 81-97 (2012).
10. A. D. Chanyshv, K. D. Litasov, S. V. Rashchenko, A. Sano-Furukawa, H. Kagi, T. Hattori, A. F. Shatskiy, A. M. Dymshits, I. S. Sharygin and Y. Higo, *Cryst. Growth Design* **18**, 3016-3026 (2018).
11. L. Ciabini, F. A. Gorelli, M. Santoro, R. Bini, V. Schettino and M. Mezouar, *Phys. Rev. B* **72**, 094108 (2005).
12. C. François, F. Denise and P. Jean - Pierre, *J. Chem. Phys.* **99**, 7300-7304 (1993).
13. A. Jagannadham and C. K. George, *J. Chem. Phys.* **55** (2), 793-796 (1971).
14. C. Baker, J. Oakley, D. Rowland, T. Hughes, Z. Aman and E. May, *Energy Fuels* **32**, 255-267 (2018).
15. A. Siahvashi, S. Z. S. Al Ghafri and E. F. May, *Fluid Phase Equilib.* **519**, 112609 (2020).
16. J. Hildebrand and R. Scott, *The solubility of nonelectrolytes*. (Reinhold Pub. Corp., New York, 1950).
17. J. M. Prausnitz, R. N. Lichtenthaler and E. G. De Azevedo, *Molecular thermodynamics of fluid-phase equilibria*. (Pearson Education, Upper Saddle River, New Jersey, 1998).

18. Infochem, (KBC Advanced Technologies, Walton-on-Thames, England, 2018).
19. C. Baker, A. Siahvashi, J. Oakley, T. Hughes, D. Rowland, S. Huang and E. F. May, *J Chem Thermodyn* **137**, 22-33 (2019).
20. C. J. H. Baker, T.J.; Rowland, D.; Oakley, J.; Aman, Z.; Frotscher, O.; May, E.F. , (Fluid Science and Resources, The University of Western Australia. <https://www.fsr.ecm.uwa.edu.au/thermofast-full/>, 2020).
21. A. Siahvashi, S. Z. S. Al Ghafri, T. J. Hughes, B. F. Graham, S. H. Huang and E. F. May, *Exp Therm Fluid Sci* **105**, 47-57 (2019).
22. A. Siahvashi, S. Z. S. Al Ghafri, B. F. Graham and E. F. May, *J Nat Gas Sci Eng* **90**, 103918 (2021).
23. J. P. M. Trusler, *J. Phys. Chem. Ref. Data* **40**, 043105 (2011).
24. M. T. Dove, *Introduction to Lattice Dynamics*. (Cambridge University Press, 1993).
25. J. H. Williams, in *Crystal Engineering* (Morgan & Claypool Publishers, 2017), pp. 1-19.
26. C. S. Hurlbut and C. Klein, *Manual of Mineralogy*. (Wiley, 1985).
27. CrystalMaker, (CrystalMaker Software Ltd, Yarnton, OX5 1PF, UK).
28. L. Lepodise, J. Horvat and R. A. Lewis, *Phys. Chem. Chem. Phys.* **15**, 20252-20261 (2013).
29. M. M. Thiery and J. M. Leger, *J. Chem. Phys.* **89**, 4255-4271 (1988).
30. C. Kittel, *Introduction to Solid State Physics*. (Wiley, 2004).
31. J. P. Poirier and A. Tarantola, *Phys. Earth Planet. Inter.* **109**, 1-8 (1998).
32. L. Vocadlo, J. Poirer and G. Price, *Am. Mineral* **85**, 390-395 (2000).
33. S. W. Kieffer, *Rev. Geophys.* **17** (1), 1-19 (1979).
34. X. Qian, in *Advances in Science and Technology of Mn+1AX_n Phases* (Elsevier, 2012), pp. 1-19.
35. R. D. Mair and D. F. Hornig, *J. Chem. Phys.* **17**, 1236-1247 (1949).
36. C. A. Swenson and W. B. Person, *J. Chem. Phys.* **33**, 56-64 (1960).
37. G. R. Anderson and W. B. Person, *J. Chem. Phys.* **36**, 62-71 (1962).
38. J. L. Hollenberg and D. A. Dows, *J. Chem. Phys.* **37**, 1300-1307 (1962).
39. M. Ito, *J. Chem. Phys.* **42**, 2844-2848 (1965).
40. I. Harada and T. Shimanouchi, *J. Chem. Phys.* **44**, 2016-2028 (1966).
41. A. R. Gee and G. W. Robinson, *J. Chem. Phys.* **46**, 4847-4853 (1967).
42. E. Bernstein, S. Colson, D. Tinti and G. Robinson, *J. Chem. Phys.* **48**, 4632-4659 (1968).
43. H. Bonadeo, M. Marzocchi, E. Castellucci and S. Califano, *J. Chem. Phys.* **57**, 4299-4303 (1972).
44. W. D. Ellenson and M. Nicol, *J. Chem. Phys.* **61**, 1380-1389 (1974).
45. P. C. Painter and J. L. Koenig, *Spectrochim. Acta A* **33**, 1019-1024 (1977).
46. R. Torre, R. Righini, L. Angeloni and S. Califano, *J. Chem. Phys.* **93**, 2967-2973 (1990).
47. M. Thiery, J. Besson and J. Bribes, *J. Chem. Phys.* **96**, 2633-2654 (1992).
48. J. Pinan, R. Ouillon, P. Ranson, M. Becucci and S. Califano, *J. Chem. Phys.* **109**, 5469-5480 (1998).
49. E. B. Wilson, *Phys. Rev.* **45** (10), 706-714 (1934).
50. A. M. Gardner and T. G. Wright, *J. Chem. Phys.* **135**, 114305 (2011).
51. A. Katrusiak, M. Podsiadło and A. Budzianowski, *Cryst. Growth Des.* **10**, 3461-3465 (2010).
52. J. D. Dunitz and R. M. Ibberson, *Angew. Chem. Int. Ed.* **47**, 4208-4210 (2008).

53. A. D. Fortes and S. C. Capelli, *Phys. Chem. Chem. Phys.* **20**, 16736-16742 (2018).
54. Z. Wu and R. M. Wentzcovitch, *Phys. Rev. B* **79**, 104304 (2009).
55. J. P. Trusler, *J. Phys. Chem. Ref. Data* **41** (3) (2012).
56. P. L. Dulong and A.-T. Petit, *Annales de Chimie et de Physique* **10**, 395 (1819).
57. E. R. Andrew and R. G. Eades, *Proc. R. Soc. London, Ser. A* **218** (1135), 537-552 (1953).
58. J. N. Andrews and A. R. J. P. Ubbelohde, *Proc. R. Soc. London, Ser. A* **228**, 435-447 (1955).
59. G. Bacon, N. t. Curry and S. Wilson, *Proc. R. Soc. London, Ser. A* **279**, 98-110 (1964).
60. W. Biltz, W. Fischer and E. Wunnenberg, *Z. Phys. Chem.* **151**, 13-55 (1930).
61. E. G. Cox and W. H. Bragg, *Proc. R. Soc. Lond. A Math. Phys. Sci.* **135** (827), 491-498 (1932).
62. E. G. Cox, D. W. J. Cruickshank and J. A. S. Smith, *Proc. R. Soc. Lond. A Math. Phys. Sci.* **247** (1248), 1-21 (1958).
63. C. J. Craven, P. D. Hatton, C. J. Howard and G. S. Pawley, *J. Chem. Phys.* **98**, 8236-8243 (1993).
64. J. Ferche, *Ann. Phys. (Leipzig)* **280**, 265-287 (1891).
65. W. Heuse, *Z. Phys. Chem.* **147A**, 266 (1930).
66. A. Heydweiller, *Ann. Phys.* **297**, 527-540 (1897).
67. V. Kozhin, *Zh. Fiz. Khim.* **28**, 566-566 (1954).
68. C. A. McConville, Y. Tao, H. A. Evans, B. A. Trump, J. B. Lefton, W. Xu, A. A. Yakovenko, E. Kraka, C. M. Brown and T. Runčevski, *Chem Comm* **56**, 13520-13523 (2020).
69. K. Ziegler and F. Ditzel, *Justus Liebigs Ann. Chem.* **473**, 194-210 (1929).
70. J. E. Ahlberg, E. R. Blanchard and W. O. Lundberg, *J. Chem. Phys.* **5**, 539-551 (1937).
71. D. H. Andrews, G. Lynn and J. Johnston, *J. Am. Chem. Soc.* **48**, 1274-1287 (1926).
72. W. F. B. Jr. and W. T. Ziegler, *J. Chem. Phys.* **10**, 740-743 (1942).
73. J. Dewar, *Proc. R. Soc. London, Ser. A* **89**, 158-169 (1913).
74. A. Diedrichs, University of Oldenburg, 2005.
75. I. Hahnenkamp, University of Oldenburg, 2008.
76. H. M. Huffman, G. S. Parks and A. C. Daniels, *J. Am. Chem. Soc.* **52**, 1547-1558 (1930).
77. O. Maass and L. J. Waldbauer, *J. Am. Chem. Soc.* **47**, 1-9 (1925).
78. Z. Nan and Z.-C. Tan, *Thermochim. Acta* **419**, 275-281 (2004).
79. W. Nernst, *Ann. Phys.* **341**, 395-439 (1911).
80. G. D. Oliver, M. Eaton and H. M. Huffman, *J. Am. Chem. Soc.* **70**, 1502-1505 (1948).
81. D. R. Stull, *J. Am. Chem. Soc.* **59**, 2726-2733 (1937).
82. C. J. Craven, P. D. Hatton and G. S. Pawley, *J. Chem. Phys.* **98**, 8244-8255 (1993).
83. L.-C. Brunel, *Chem Phys* **37**, 201-210 (1979).
84. J. C. W. Heseltine, D. W. Elliott and O. B. W. Jr., *J. Chem. Phys.* **40**, 2584-2587 (1964).
85. K. Růžička, M. Fulem and C. Červinka, *J. Chem. Thermodyn.* **68**, 40-47 (2014).
86. J. T. Barker, *Z Phys Chem* **71U**, 235-253 (1910).
87. S. U. Choi and H. C. Brown, *J. Am. Chem. Soc.* **88**, 903-909 (1966).

88. C. G. De Kruif and C. H. D. Van Ginkel, *J Chem Thermodyn* **9**, 725-730 (1977).
89. C. G. De Kruif, *J Chem Thermodyn* **12**, 243-248 (1980).
90. V. Deitz, *J. Am. Chem. Soc.* **55**, 472-475 (1933).
91. H. Ha, J. Morrison and E. Richards, *J. Chem. Soc., Faraday Trans. 1* **72**, 1051-1057 (1976).
92. A. W. Jackowski, *J. Chem. Thermodyn.* **6**, 49-52 (1974).
93. I. Kiss, G. Jakli and H. Illy, *Acta Chim. Acad. Sci. Hung* **71**, 59-74 (1972).
94. K. Liu and R. M. Dickhut, *Chemosphere* **29**, 581-589 (1994).
95. G. Milazzo, *Ann. Chim. (Rome)* **46**, 1105 (1956).
96. G. Milazzo, *Chem. Ing. Tech.* **28**, 646-654 (1956).
97. N. R. K. Miljevic, Z. V.; Dokic, V. R.; Pupezin, J. D., *Glas. Hem. Drus. Beograd* **42**, 243 (1977).
98. C. F. Mündel, *Z. Phys. Chem* **85U**, 435-465 (1913).
99. D. Radulescu and M. Alexa, *Bull. Soc. Chim. Romania* **20A**, 89-113 (1938).
100. R. P. Rastogi, J. Nath and J. Misra, *J Phys Chem* **71**, 1277-1286 (1967).
101. S. Young, *Sci. Proc. R. Dublin Soc.* **12**, 374-443 (1910).
102. E. G. Cox and J. A. S. Smith, *Nature* **173**, 75 (1954).
103. M. Azreg-Aïnou, A. Hüseyinov and B. İbrahimoglu, *J. Chem. Phys.* **124**, 204505 (2006).
104. M. Azreg-Aïnou, A. Hüseyinov and B. İbrahimoglu, *J. Chem. Phys.* **125**, 099901 (2006).
105. P. W. Bridgman, *Phys. Rev.* **3**, 153-203 (1914).
106. W. Xu, R. Zhu, Y. Tian, H. Li and H. Li, *J. Chem. Eng. Data* **52**, 1975-1978 (2007).
107. D. B. Robinson and D.-Y. Peng, 1978.
108. A. Péneloux, E. Rauzy and R. Fréze, *Fluid Phase Equilib.* **8**, 7-23 (1982).
109. Infochem, (KBC Advanced Technologies, Walton-on-Thames, England, 2017).
110. J. Osugi, K. Shimizu and A. Onodera, *Rev Phys Chem Jpn* **34** (2), 97-101 (1965).
111. E. A. Block, *Z. Phys. Chem* (1913).
112. G. Tammann, University of Leipzig, 1903.
113. P. W. Bridgman, *Proc. Am. Acad. Arts Sci.* **77**, 129-146 (1949).
114. L. Deffet, *Bull. Soc. Chim. Belg.* **44**, 41 (1935).
115. L. Deffet, *Bull. Soc. Chim. Belg.* **51**, 237 (1942).
116. U. Domańska and P. Morawski, *J. Chem. Thermodyn.* **37**, 1276-1287 (2005).
117. U. Domańska and P. Morawski, *Green Chem* **9**, 361-368 (2007).
118. A. Easteal, L. Woolf and F. Wilson, *Int. J. Thermophys.* **6**, 275-284 (1985).
119. P. Figuière, A. H. Fuchs, M. Ghelfenstein and H. Szwarc, *J Phys Chem Solids* **39**, 19-24 (1978).
120. A. Fruhling, *Ann. Phys.* **12**, 401-480 (1951).
121. M. Ghelfenstein and H. Szwarc, *Chemical Physics Letters* **32**, 93-98 (1975).
122. G. A. Hulett, *Z. Phys. Chem* **28U**, 629 (1899).
123. T. Makita and T. Takagi, *Rev Phys Chem Jpn* **38**, 41-49 (1968).
124. K. Nagaoka and T. Makita, *Int J Thermophys* **8**, 415-424 (1987).
125. J. Osugi, K. Shimizu, K. Yasunami, M. Moritoki and A. Onodera, *Rev Phys Chem Jpn* **38**, 90-95 (1968).
126. P. P., 1976.
127. L. T. M. P. Pruzan, A. Souldard, in *High-Pressure Science and Technology*, edited by K. D. Timmerhaus and M. S. Barber (Springer, University of Colorado, Boulder, Colorado, USA, 1979), Vol. 1, pp. 368-378.

128. T. Sun, P. Kortbeek, S. Biswas, N. Trappeniers and J. Schouten, *Ber. Bunsen-Ges. Phys. Chem.* **91**, 1013-1017 (1987).
129. Y. Tanaka and M. Kawakami, *Fluid Phase Equilib.* **125**, 103-114 (1996).
130. C. Yokoyama, T. Ebina and S. Takahashi, *Fluid Phase Equilib.* **84**, 207-223 (1993).
131. A. Budzianowski and A. Katrusiak, *Acta Cryst. B* **62**, 94-101 (2006).
132. D. W. M. Hofmann and L. N. Kuleshova, *Cryst. Growth Des.* **14**, 3929-3934 (2014).
133. P. W. Bridgman, *J Chem Phys* **9** (11), 794-797 (1941).
134. P. W. Bridgman, presented at the *Proc. Am. Acad. Arts Sci.* , 1942 (unpublished).
135. R. G. Ross, P. Andersson and G. Bäckström, *Mol. Phys.* **38**, 527-533 (1979).
136. A. H. Fuchs, P. Pruzan and L. Ter Minassian, *J. Phys. Chem. Solids* **40**, 369-374 (1979).
137. P. Pruzan, D. H. Liebenberg and R. L. Mills, *J Phys Chem Solids* **47**, 949-961 (1986).